

AnyCalib: On-Manifold Learning for Model-Agnostic Single-View Camera Calibration

Javier Tirado-Garín Javier Civera
I3A, University of Zaragoza
{j.tiradog, jcivera}@unizar.es

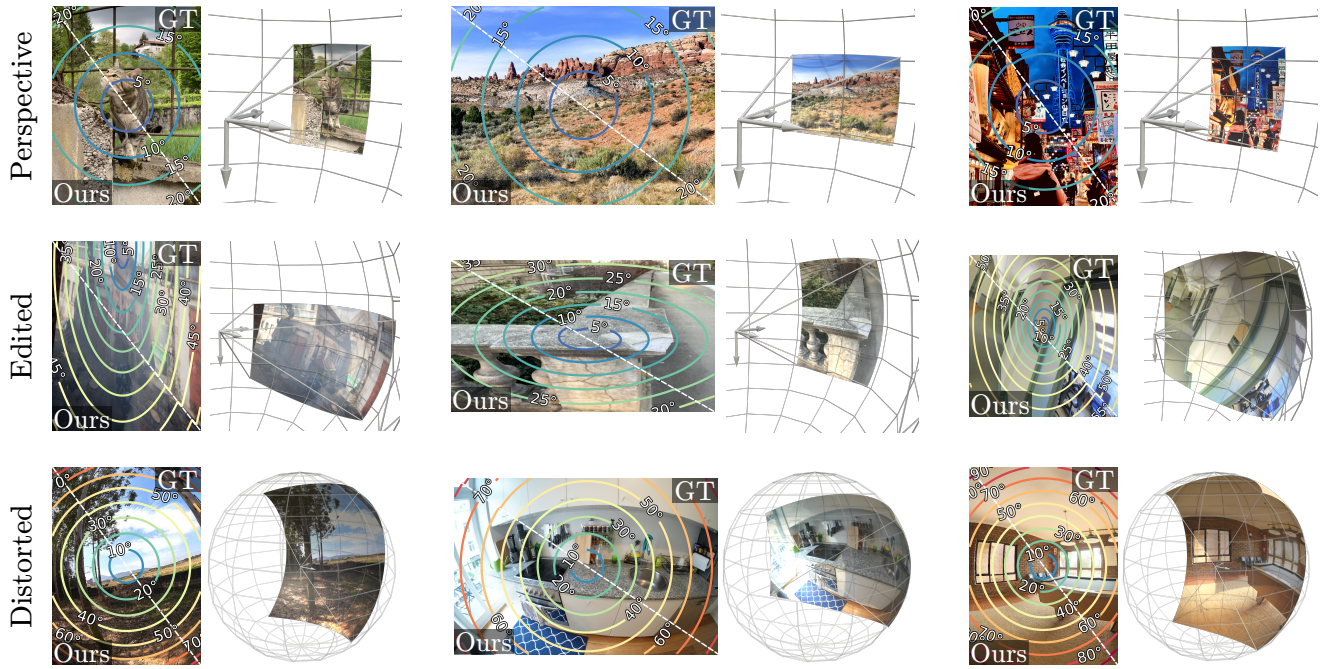


Figure 1. **We introduce AnyCalib**, the first model-agnostic single-view camera calibration method. AnyCalib works with perspective, edited and distorted images and has flexibility in selecting the camera model at runtime. The left subfigures compare ground-truth and estimated *polar angles* (angle between the optical axis and the ray direction of each pixel) on *in-the-wild* images. Despite the wide range of field-of-view and the absence of perspective cues in natural and close-up photos, AnyCalib accurately calibrates each camera. It does so by framing the calibration process as the regression of the rays corresponding to each pixel, which we represent on the right subfigures.

Abstract

We present *AnyCalib*, a method for calibrating the intrinsic parameters of a camera from a single *in-the-wild* image, that is agnostic to the camera model. Current methods are predominantly tailored to specific camera models and/or require extrinsic cues, such as the direction of gravity, to be visible in the image. In contrast, we argue that the perspective and distortion cues inherent in images are sufficient for model-agnostic camera calibration. To demonstrate this, we frame the calibration process as the regression of the rays corresponding to each pixel.

We show, for the first time, that this intermediate representation allows for a closed-form recovery of the intrinsics for a wide range of camera models, including but not limited to: pinhole, Brown-Conrady and Kannala-Brandt. Our approach also applies to edited—cropped and stretched—images. Experimentally, we demonstrate that *AnyCalib* consistently outperforms alternative methods, including 3D foundation models, despite being trained on orders of magnitude less data. Code is available at <https://github.com/javrtg/AnyCalib>.

1. Introduction

Camera calibration is the task of estimating the mapping from image points to their corresponding *ray* directions [33]. Although alternatives exist [31, 73], this mapping is typically modeled using a set of *intrinsic parameters* (or *intrinsic*s for short), which depend on the chosen camera model [52, 80, 85]. Accurate intrinsics are crucial for many computer vision tasks that aim to recover the 3D geometry of an observed scene, as *e.g.*, in SLAM [15, 57, 58], Structure-from-Motion (SfM) [5, 61, 72] and novel-view synthesis [40, 56].

The literature on calibration from multiple images is vast and mature. The most accurate methods assume *controlled* scenes, where a calibration target with known geometry is observed [12, 27, 52, 71, 84, 99]. Intrinsics can also be estimated in non-controlled scenes as part of SfM [5, 61, 72] and visual SLAM [17, 32, 59], provided that sufficient geometric constraints are present across images/views.

However, some applications require known intrinsics for *in-the-wild single-view* tasks, like depth [9, 24, 37, 50, 96] and normal [8] map estimations. Moreover, in non-controlled scenes, multi-view geometric methods fail when the intrinsics are insufficiently constrained, due to, *e.g.*, limited visual overlap across views. In such cases, single-view calibration methods are an attractive alternative. Rather than multi-view constraints, they use alternative geometric [6, 51, 64, 93] and learned [36, 38, 53, 86] cues present in a single input image.

They, however, have limitations. Purely geometric approaches excel in structured scenes, where their assumptions, *e.g.* the presence of parallel lines, are satisfied, but catastrophically fail otherwise [86]. On the other hand, methods trained to directly predict intrinsics [35, 38, 53] only learn a subset of image projections, which impacts their accuracy in out-of-domain ones. Additionally, they often condition the calibration with extrinsic cues, such as the direction of gravity and the image location of the horizon [38, 53, 86]. Thus, their accuracy decreases when these cues are not visible. Finally, current single-view calibration methods, geometric and learned, are tailored to specific camera models, either by design [36, 52, 53, 64, 93] and/or during training [38, 86].

To address these limitations, we propose AnyCalib, a novel single-view camera calibration method. Our main contributions are:

- AnyCalib is the first *model-agnostic* single-view camera calibration model. We frame the calibration process as the regression of the rays corresponding to each pixel. We show, that this representation is model-agnostic since it allows for a closed-form recovery of the intrinsics for a wide range of camera models, without conditioning its training nor design on specific ones. Thus, our method also applies to *edited* (stretched and cropped) images.

Some qualitative results are shown in Fig. 1.

- We introduce *Field of View (FoV) fields*, a novel intermediate representation that is bijective to the rays of each pixel. In contrast to ray (or incidence [100]) fields, FoV fields are a minimal Euclidean representation that is directly related to the image content. We demonstrate that this representation leads to improved accuracy.
- Since our approach is not coupled with extrinsic cues, we extend the OpenPano dataset [86] with panoramas that do not need to be aligned with the gravity direction. This also allows us to show that AnyCalib is scalable, as this extended dataset leads to improved accuracy.
- We propose an alternative “light” DPT decoder [67] that does not use expensive transposed convolutions to upsample the predictions. This improves the model efficiency.
- Finally, AnyCalib sets a new state-of-the-art across perspective, edited and distorted images, while having flexibility in selecting camera models at runtime.

2. Related Work

Purely geometric approaches calibrate intrinsics using constraints derived from low-level visual cues. Vanishing points and lines [33] are the most common [6, 16, 21, 44, 51, 64, 66, 93] and are typically fitted to line detections [30, 63] that are parallel and/or coplanar, using *e.g.* RANSAC-based methods [42, 51, 64, 92]. These approaches, thus, have strict requirements: parallel lines must be detected and vanishing points may need to form a Manhattan frame [21, 44, 52, 64]. Geometric approaches are thus accurate in structured scenes but fail otherwise, even in urban imagery [49, 86]. Moreover, they are restricted to the pinhole [16, 21, 44, 64] or division [6, 51, 93] camera models. In contrast, AnyCalib is model-agnostic and more robust since it does not rely only on the previous low-level cues. Our proposed intermediate representation and training dataset are appropriate for scenes lacking them, as shown in Fig. 1.

End-to-end learned approaches train deep neural networks to directly predict the intrinsics of a certain camera model, such as pinhole [38, 46, 75, 79], radial [53], UCM [10, 35, 36] or alternative proposed ones [87, 88]. They are generally more robust than geometric approaches [86], but at the expense of *accuracy*, as they do not impose geometric constraints, and *flexibility*, since adapting to other cameras would require retraining and architectural changes. Additionally, they often rely on extrinsic cues, such as the direction of gravity [38], the image location of the horizon [53] or lines converging at the horizon and zenith [46]. Thus, they lose accuracy if these cues are not visible. In contrast, AnyCalib is not tied to a specific camera model or extrinsic cues and its accuracy is comparable or better than geometric approaches thanks to imposing geometric constraints.

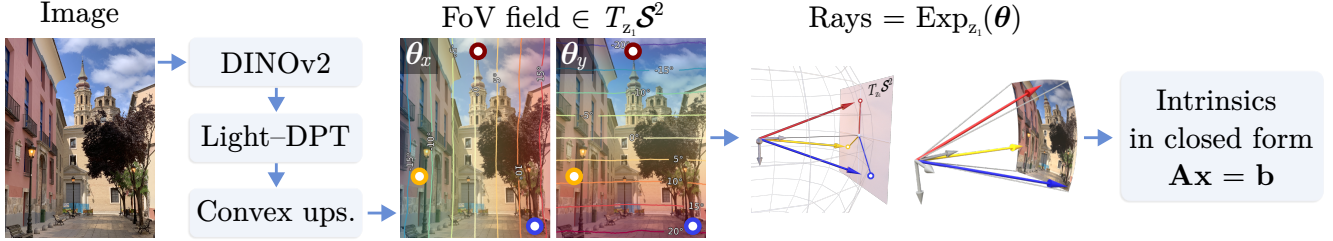


Figure 2. **Method.** AnyCalib predicts dense FoV fields (Sec. 3.1) using a transformer backbone and a light CNN decoder (Sec. 3.3). FoV fields are supervised on the unit sphere, in the tangent plane at the optical axis of the camera. This representation is bijective to rays, which along their corresponding image coordinates, allow a closed-form model-agnostic calibration of a wide range of camera models (Sec. 3.2).

Hybrid approaches train an intermediate representation that is used to fit the intrinsics by imposing geometric constraints [18, 34, 86, 100], in a similar spirit to previous works on distortion [48] and rotation [94] estimation. WildCam [100] and DiffCalib [34] directly estimate the ray directions for each pixel, restricting their implementation to perspective (pinhole) and edited images. Dal Cin et al. [18] also propose regressing rays, using a polar input representation that restricts their method to non-edited images. It requires heuristics [78] to fit the intrinsics and its training uses a highly non-linear reprojection error [85] as loss function, which can difficult its convergence. GeoCalib [86] iteratively optimizes the intrinsics from learned perspective fields [38], that are weighted by uncertainties trained by supervising intrinsics. This generally leads to more accurate local minimums but increases the risk of overfitting. Additionally, the accuracy of perspective fields decreases when the horizon and gravity direction are not perceivable [86].

In contrast to all previous methods, AnyCalib works with *perspective, edited* and *distorted* images and is not tied to extrinsic cues. Different to methods that also predict rays, AnyCalib uses a minimal Euclidean intermediate representation that leads to improved accuracy and that also applies to edited images. Additionally, we show, for the first time, that rays allow for a *closed-form solution* of the intrinsics for a wide range of camera models.

3. Method

Given an $H \times W$ input image, AnyCalib densely predicts FoV fields (Sec. 3.1), which are bijective to the ray directions corresponding to each pixel. From these rays and image coordinates, we obtain, in closed-form, the globally-optimal intrinsics of the camera model of choice (Sec. 3.2).

3.1. FoV field as intermediate representation

Current target representations. The unit rays corresponding to each pixel, lie on the \mathcal{S}^2 manifold or unit sphere, which is not closed under linear combinations of its elements. Thus, common operations, such as the upsampling done in WildCam [100] to densely regress rays, are

not well-defined [82]. DiffCalib [34] and Dal Cin et al. [18] use better-defined representations, but they are either limited by design to moderate Field-of-Views [34]—pinhole unprojections, or to non-edited images [18]—perfect square pixels and a centered principal point.

FoV cue. On the other hand, instead of directly regressing rays, multiple works [36, 43, 46, 53, 62] identify the Field-of-View (FoV) as an image cue that is inherent and directly perceivable from the image content. However, these works limit the FoV prediction to just a single value—the maximum angular extent of the image. As such, they cannot densely impose geometric constraints.

FoV fields. To address these limitations, we propose *FoV fields* as intermediate representation. As depicted in Fig. 2, FoV fields correspond to elements in the tangent space $T_{z_1} \mathcal{S}^2$ [13] at the optical axis $\mathbf{z}_1 := [0, 0, 1]^\top \in \mathcal{S}^2$:

$$T_{z_1} \mathcal{S}^2 = \{\mathbf{v} \in \mathbb{R}^3 \mid \mathbf{z}_1^\top \mathbf{v} = 0\}. \quad (1)$$

Any ray $\mathbf{p} \in \mathcal{S}^2$ can be uniquely mapped to $T_{z_1} \mathcal{S}^2$ via the *logarithm map* $\text{Log}_{z_1} : \mathcal{S}^2 \rightarrow T_{z_1} \mathcal{S}^2$ [13]:

$$\mathbf{v} = \text{Log}_{z_1}(\mathbf{p}) = \arccos(\mathbf{z}_1^\top \mathbf{p}) \frac{\mathbf{p} - (\mathbf{z}_1^\top \mathbf{p}) \mathbf{z}_1}{\|\mathbf{p} - (\mathbf{z}_1^\top \mathbf{p}) \mathbf{z}_1\|}, \quad (2)$$

which implies that

$$\theta := \|\text{Log}_{z_1}(\mathbf{p})\| = \arccos(\mathbf{z}_1^\top \mathbf{p}), \quad (3)$$

which is precisely the *polar angle* θ corresponding to the unit ray \mathbf{p} , *i.e.*, the angle between \mathbf{p} and the optical axis \mathbf{z}_1 . In other words, FoV fields encode the FoV¹ (double of θ) corresponding to each pixel.

However, $\mathbf{v} \in T_{z_1} \mathcal{S}^2$ are *non-minimal, constrained* vectors (Eq. (1)). Thus, to obtain a *minimal, unconstrained* target representation $\boldsymbol{\theta} \in \mathbb{R}^2$ to learn by our network, we use local coordinates [20], *i.e.* we express them in a 2D coordinate system located in the tangent plane. We use axes

¹The term *FoV* commonly refers to the *maximum* angular extent of an image. In this paper, we slightly extend this definition for referring to the angular extent *up to any pixel*.

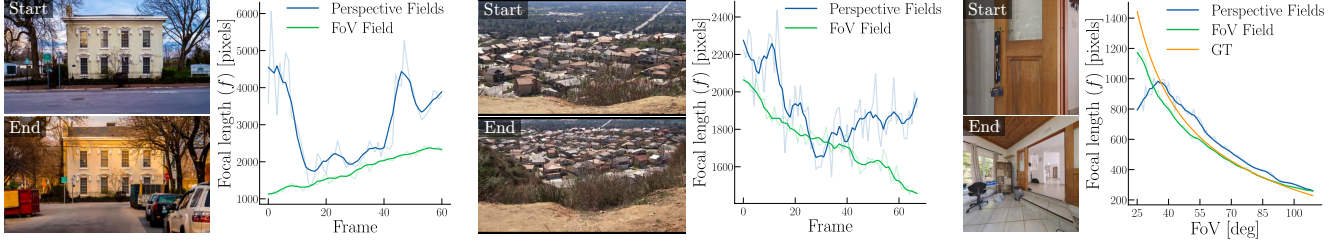


Figure 3. **Perspective vs FoV fields.** We show focal length (f) estimates by GeoCalib [86] and AnyCalib. Sequences depict dolly-zooms, where f continuously increases (left) or decreases (middle) while the camera moves to keep a focused object visually unchanged, and a zoom-out (right) where f decreases. AnyCalib correctly predicts these tendencies, while GeoCalib struggles since the horizon is occluded (left), not visible (middle) or there is insufficient image information (right). FoV fields are more robust as they rely on image content rather than extrinsic cues. None of the images were seen during training. Media sources, from left to right: [77], [74] and [98].

parallel to the camera’s x - and y -axes. This change of basis² simply takes the first two elements of \mathbf{v} :

$$\boldsymbol{\theta} := \mathbf{B}_{xy} \mathbf{v}, \quad \mathbf{B}_{xy} = \begin{bmatrix} 1 & 0 & 0 \\ 0 & 1 & 0 \end{bmatrix}. \quad (4)$$

Ground-truth values of $\boldsymbol{\theta} \in \mathbb{R}^2$ are used for training. They are obtained from ground-truth rays as

$$\boldsymbol{\theta} = \mathbf{B}_{xy} \text{Log}_{\mathbf{z}_1}(\mathbf{p}) = \frac{\theta}{\sin \theta} \mathbf{B}_{xy} \mathbf{p}, \quad (5)$$

since $\mathbf{B}_{xy} \mathbf{z}_1 = \mathbf{0}$ and³ $\|\mathbf{p} - (\mathbf{z}_1^\top \mathbf{p}) \mathbf{z}_1\| = \sin \theta$.

Given dense $\boldsymbol{\theta}$ predictions by our network, we map them to unit rays using the *exponential map*. It is defined as [13]:

$$\mathbf{p} = \text{Exp}_{\mathbf{z}_1}(\mathbf{v}) = \cos(\theta) \mathbf{z}_1 + \frac{\sin \theta}{\theta} \mathbf{v}, \quad (6)$$

which under our representation, simplifies to

$$\mathbf{p} = \text{Exp}_{\mathbf{z}_1}(\mathbf{B}_{xy}^\top \boldsymbol{\theta}) = \begin{bmatrix} \frac{\sin \theta}{\theta} \boldsymbol{\theta} \\ \cos \theta \end{bmatrix}. \quad (7)$$

Importance of image content. State-of-the-art representations tied to extrinsic cues [38, 86] often struggle when these are not clearly visible. In contrast, FoV fields are more robust, as they rely more on the image content and relative position of the elements within a scene, as shown in Fig. 3.

3.2. Model-agnostic calibration from rays

Projection models. Differently to current single-view calibration methods, we altogether consider: 1) projection models with radial distortion [52, 85], 2) non-square image pixels, *i.e.*, different focal lengths, $\mathbf{f} := [f_x, f_y]^\top$, $a := f_y/f_x \neq 1$, for each image axis, 3) a non-centered principal point, $\mathbf{c} := [c_x, c_y]^\top$, *i.e.* we do not fix \mathbf{c} to $[W/2, H/2]^\top$,

²Note that $\theta = \|\boldsymbol{\theta}\|$ since \mathbf{v} has a null z -component.

³Since $\mathbf{z}_1, \mathbf{p} \in \mathcal{S}^2$, this implies that $\|\mathbf{p} - (\mathbf{z}_1^\top \mathbf{p}) \mathbf{z}_1\| = (1 - (\mathbf{z}_1^\top \mathbf{p})^2)^{1/2} = (1 - \cos^2 \theta)^{1/2} = \sin \theta$.

and 4) different, forward and backward [52], camera models that can be freely chosen at runtime.

Under these characteristics, a general *forward* projection function, $\pi : \mathcal{S}^2 \rightarrow \Omega \subset \mathbb{R}^2$, mapping rays in the unit sphere $\mathbf{p} := [X, Y, Z]^\top \in \mathcal{S}^2$ to image coordinates $\mathbf{x} := [u, v]^\top \in \Omega$ in the image domain Ω , is given by⁴

$$\pi(\mathbf{p}) = \begin{bmatrix} u \\ v \end{bmatrix} = f \phi(R, Z) \begin{bmatrix} X \\ aY \end{bmatrix} + \begin{bmatrix} c_x \\ c_y \end{bmatrix}, \quad (8)$$

where $\phi(R, Z)$ is a camera-model specific function of the ray radius $R = \sqrt{X^2 + Y^2}$ and its Z component. On the other hand, a general *backward* [52] unprojection function, $\pi^{-1} : \Omega \rightarrow \mathcal{S}^2$, is given by

$$\pi^{-1}(\mathbf{x}) = \begin{bmatrix} X \\ Y \\ Z \end{bmatrix} = \lambda \begin{bmatrix} m_x \\ m_y \\ \psi(r) \end{bmatrix}, \quad (9)$$

where λ is a unit-norm normalization constant, $\psi(r)$ is a function that depends on the chosen backward model and:

$$\begin{bmatrix} m_x \\ m_y \end{bmatrix} := \begin{bmatrix} (u - c_x)/f \\ (v - c_y)/(af) \end{bmatrix}, \quad r := \sqrt{m_x^2 + m_y^2}. \quad (10)$$

Principal point and pixel aspect ratio. Given the image coordinates \mathbf{x} and their predicted ray coordinates, we can directly recover \mathbf{c} and a in closed-form. Either by subtracting \mathbf{c} from \mathbf{x} in Eq. (8) and then dividing their entries, or by dividing the first two entries of Eq. (9), the model-specific functions ϕ and ψ , and focal length f disappear, leading to the simplified constraint:

$$uY a - Y a c_x + X c_y = vX, \quad (11)$$

which is well defined for all $\mathbf{p} \in \mathcal{S}^2$, $\mathbf{x} \in \Omega$, and depends linearly on a , $a c_x$ and c_y . Thus we can recover \mathbf{c} and a in closed-form solving the corresponding overconstrained linear system and undoing the reparameterization in $a c_x$.

⁴To alleviate the notation, we define $f := f_x$, so $f_y = af = a f_x$.

Model	Model-specific function	Linear constraints	Unknowns
Pinhole	$1/Z$	$R_a f = Z r_c$	f
Brown-Conrady [14]	$(1/Z)(1 + \sum_{n=1}^N k_n (R/Z)^{2n})$	$r_c Z g - R_a \sum_{n=1}^N k_n (R/Z)^{2n} = R_a$	$g := 1/f, \{k_1 \dots k_N\}$
Kannala-Brandt [39]	$\phi(R, Z) = (\theta + \sum_{n=1}^N k_n \theta^{2n+1})/R$	$R r_c g - R_a \sum_{n=1}^N k_n \theta^{2n+1} = R_a \theta$	$g := 1/f, \{k_1 \dots k_N\}$
UCM [29, 55]	$(\xi d + Z)^{-1}$	$R_a f - r_c d \xi = r_c Z$	f, ξ
EUCM [†] [41]	$(\alpha \sqrt{\beta R^2 + Z^2} + (1 - \alpha)Z)^{-1}$	$r^2 R^2 \gamma + 2rZ(rZ - R)\alpha = (R - rZ)^2$	$\gamma := \alpha^2 \beta, \alpha$
Division [26, 45]	$\psi(r) = 1 + \sum_{n=1}^N k_n r^{2n}$	$R_a (f + \sum_{n=1}^N k'_n r_{ca}^{2n}) = Z r_c$	$f, \{k'_1 \dots k'_N\}, k'_n := k_n / f^{2n-1}$

Table 1. **Implemented camera models.** Once the principal point \mathbf{c} and pixel aspect-ratio a are known via Eq. (11), the Eqs. (8) and (9) become linear w.r.t. the remaining intrinsics—using the reparameterizations of the rightmost column. Our implementation allows a variable number of distortion coefficients, k , in models that allow so [14, 26, 39, 45]. [†]For EUCM [41] we operate slightly differently since linearity in Eq. (8) is lost when f is unknown. Instead, to estimate f , we use a proxy camera model [39] that leads to practically the same focal length value [52, 85]. *Auxiliary definitions* for expressing the linear constraints (see Supp. D): $R_a := \sqrt{X^2 + a^2 Y^2}$, $r_c := \|\mathbf{x} - \mathbf{c}\|$, $\theta := \text{atan2}(R, Z)$, $d := \sqrt{R^2 + Z^2}$ and $r_{ca}^2 := (u - c_x)^2 + (v - c_y)^2 / a^2$.

Remaining intrinsics. Given estimations⁵ for a and \mathbf{c} , the Eqs. (8) and (9) become linear with respect to the remaining intrinsics of a wide range of commonly used camera models [52, 85]. This is shown in Tab. 1, where we also indicate the currently implemented models, but our formulation can also be applied to others, *e.g.* the WoodScape model [97] or the ones proposed by Scaramuzza et al. [70] and Urban et al. [84]. Among them, UCM [55] and EUCM [41] require special care, as their parameters are bounded ($\xi \geq 0$, $\alpha \in [0, 1]$, $\beta > 0$). Since the number of bounds is limited, they can be efficiently enforced using a simplified active set method [76], that checks, when needed, which bounds need to be active. Experimentally, we did not find it necessary to enforce $f > 0$ as it is well constrained from the dense 2D-3D correspondences between rays and image points.

Final refinement. The previous closed-form solutions are globally optimal in an *algebraic* parameter space that allows a linear recovery of the intrinsics, but the optimized quantity is not interpretable. Thereby, as the final stage of our method, we iteratively optimize a nonlinear *geometric* quantity, starting from the previous global optimum. Specifically, we minimize the angular distance between the rays predicted by the network and those corresponding to the intrinsics, using five Gauss-Newton [83] iterations.

3.3. Implementation

Architecture and training. We use a ViT-L backbone [22] pretrained by DINOv2 [60]. Our CNN decoder is based on DPT [67] which we modify to not use expensive transposed convolutions. Instead, we regress FoV fields (Sec. 3.1) at 1/7 of the input resolution and finally upsample them to input resolution using convex upsampling [81]. The back-

⁵Estimating first a and \mathbf{c} leads to a unified formulation for obtaining intrinsics in closed-form across the implemented models. However, *all* intrinsics of the pinhole, BC [14] and KB [39] models can be obtained in one single step since manipulations of Eq. (8) are linear on them.

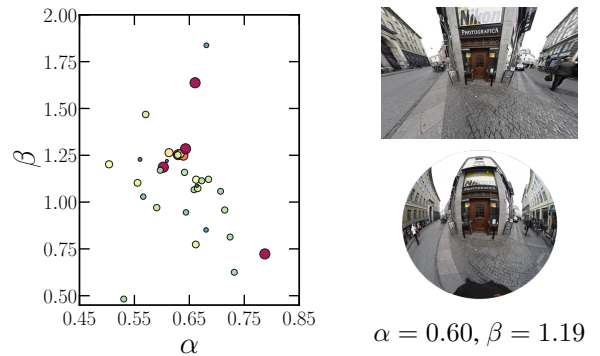


Figure 4. **Real-world sample of EUCM intrinsics.** The LensFun database [4] contains a wide range of calibrated lenses. We consider its *fish-eye* lenses and map (see Supp. B) their parameters to the EUCM’s α and β [41] to define its training bounds. (left) Resulting distribution, colored by vFoV, which ranges from 50° to $> 180^\circ$. (right) Undistortion using the mapped α and β on an image (from [68]) captured with a Nikon AI-S Fisheye-Nikkor lens.

bone and decoder use an initial learning rate of 6×10^{-6} and 6×10^{-5} , respectively. We use the AdamW [54] optimizer, with a learning rate that is linearly warmed up during the first 10^3 steps and decayed with a factor of 0.3 at 10^4 and 3×10^4 steps. We use the same augmentations of [86] and a batch size of 24 images with resolution of 320^2 pixels and aspect ratios uniformly sampled $\in [0.5, 2.0]$. We train for 40 epochs during 1 day with 3 NVIDIA V100 GPUs. Since estimating the principal point, arbitrarily placed in the image is an ill-posed problem [19, 72], for edited (stretched and cropped) images, we train a different model: we do the same as before, except that, following [34, 100], the geometric transformations correspond to uniformly sampling the pixel aspect-ratio $\in [0.5, 2]$ and an image crop of at most half its size.

We supervise the elements, θ , of the FoV field predic-

tions using a L1 loss function:

$$\mathcal{L} = \frac{1}{HW} \sum_i^{HW} \|\theta_{\text{GT}, i} - \theta_i\|_1. \quad (12)$$

Values of θ_{GT} are obtained with Eq. (5) using ray directions/unprojections obtained with ground-truth intrinsics.

Inference. AnyCalib calibrates a camera in $\sim 25\text{ms}$ in a RTX 4090. At inference, we resize and center-crop the image to the closest resolution and aspect seen during training.

Training data. Our dataset extends OpenPano [86], which consists of 2557 panoramas used to synthetically generate images with fine-grained control over the intrinsics and camera rotation. However, since GeoCalib [86] supervises extrinsic parameters, the panoramas need to be aligned with the gravity direction. AnyCalib does not have this restriction, thus we extend OpenPano to 4055 unconstrained and freely-available panoramas from the Laval Indoor dataset [11, 28], PolyHaven [98], HDRmaps [3], AmbientCG [1] and BlenderKit [2].

As detailed in Supp. B, we create four datasets: OP_p , OP_r , OP_d and OP_g , each used to separately train AnyCalib. They differ on the type of images sampled from panoramas:

- OP_p : Perspective (pinhole), following [86],
- OP_r : Distorted (using [14]), also following [86],
- OP_d : Distorted [14] and strongly distorted [41],
- OP_g : General *i.e.* perspective, distorted and strongly distorted.

Both OP_d and OP_g are motivated by the limited distortion allowed by the Brown-Conrady camera model [47, 85]. In contrast, EUCM accurately models strong distortions [41, 52, 85]. OP_g allows us to demonstrate that AnyCalib, trained on general projections, outperforms models trained on specific ones. The sampling of EUCM intrinsics is based on real-lens values extracted from the public LensFun database [4] (Fig. 4). Each training dataset consists of 54k images. See Supp. B for more details.

4. Experiments

We evaluate the calibration accuracy of AnyCalib on perspective, edited and distorted images across a wide range of benchmarks, using images not seen during training. We ablate our design choices in Supp. A and present additional qualitative results in Supp. E.

4.1. Perspective images

Metrics for measuring calibration accuracy should be *agnostic* to the chosen camera model. Otherwise, methods predicting different camera models cannot be fairly compared. A notable example is Perceptual [36], which predicts UCM [55] intrinsics. This model, as well as the majority of models, has a focal length, f , parameter. However, its

values, while correct, can be an order of magnitude different than its counterpart in other models. We show this in Supp. C. Because of this, we use model-agnostic metrics. As it is standard [38, 86], we report median errors and the Area Under the recall Curve (AUC) up to $1/5/10^\circ$ for the hFoV and vFoV, which we compute in a model-agnostic way (Supp. C). We also report the median of the mean re-projection (RE) and angular unprojection (AE) errors whose mean is computed within a uniform $H \times W$ image grid.

Datasets We follow GeoCalib [86] and evaluate on: i) Stanford2D3D [7] which consists of image samples from panoramic images captured inside university buildings, ii) TartanAir’s [91] photo-realistic renderings of scenes with changing light and various weather conditions, iii) MegaDepth’s [49] crowd-sourced images of popular landmarks, with cameras calibrated with SfM, and iv) LaMAR [69], which is an AR dataset for localization, captured over multiple years in university buildings and a city center.

Baselines We consider state-of-the-art methods that calibrate a camera from a single image: GeoCalib [86], Perceptual [36], WildCam [100] and DiffCalib [34]. We also compare AnyCalib with the 3D foundation models DUST3R [90], UniDepth [65] and MoGe [89], which either directly predict intrinsics [65], or predict 3D pointmaps that can be used to calibrate a camera [89, 90]. These foundation models are trained on > 3 million images. Among the baselines, WildCam and DiffCalib also regress rays as in our method. Dal Cin et al. [18] also predict rays, however, we could not evaluate it since it does not have public weights and we could not successfully retrain it.

Results in Tab. 2 show that $\text{AnyCalib}_{\text{pinhole}}$ and $\text{AnyCalib}_{\text{gen}}$, trained on OP_p and OP_g , respectively, outperform alternative single-view calibration methods. It also performs similar or better than 3D foundation models [89, 90], despite AnyCalib is trained on only 54k images and is not tied to perspective projections. We show results for distorted images in Sec. 4.2, that [89, 90] cannot handle.

4.2. Distorted images

Metrics. We consider the same metrics as in Sec. 4.1.

Datasets. We follow [86] and evaluate on distorted images from MegaDepth [49]. Since their distortion is limited, we also evaluate on subsets of 2000 randomly sampled images from the indoor DSLR sequences of ScanNet++ [95], and from the last 16 outdoor and indoor sequences⁶ of the SLAM dataset from [23], which we refer to as Mono.

Baselines. We consider methods evaluated in Sec. 4.1 that work with distorted images: Perceptual [36] and GeoCalib [86]. We also consider SVA [51], which is a geometric

⁶Which are the ones without black borders caused by the absence of light hitting the image sensor. No method has been trained with this effect.

	Method	AE ↓ [°]	RE ↓ [pix]	vFoV [°]			hFoV [°]				
				error ↓	AUC@1/5/10 ↑		error ↓	AUC@1/5/10 ↑			
Stanford2D3D [7]	Perceptual _{TPAMI'23} [36]	4.67	48.81	10.52	5.60	15.20	27.10	11.35	4.90	13.70	24.90
	WildCam _{NeurIPS'23} [100]	5.46	58.00	10.26	5.20	13.60	25.70	13.97	3.30	8.80	18.00
	DUST3R _{CVPR'24} [90]	2.39	27.09	5.34	10.70	26.10	43.80	6.07	9.60	23.50	40.30
	UniDepth _{CVPR'24} [65]	6.55	73.60	14.65	3.20	8.50	17.20	16.72	2.80	7.70	15.00
	GeoCalib _{ECCV'24} [86]	1.45	15.16	3.23	17.40	39.90	59.40	3.53	15.60	37.20	56.50
	DiffCalib _{AAAI'25} [34]	6.35	82.25	13.63	4.30	10.80	20.30	16.49	3.70	8.70	17.00
	MoGe _{CVPR'25} [89]	1.92	21.60	4.33	16.10	33.70	49.50	4.99	14.00	30.30	46.00
	AnyCalib_{pinhole} (Ours)	1.13	12.11	2.55	21.20	46.80	64.60	2.88	19.50	43.30	61.80
AnyCalib_{gen} (Ours)	1.30	13.90	2.95	20.80	43.60	61.60	3.24	18.60	40.30	58.90	
TartanAir [91]	Perceptual _{TPAMI'23} [36]	3.54	28.47	8.01	4.80	28.00	39.40	8.37	4.90	28.60	38.80
	WildCam _{NeurIPS'23} [100]	7.40	83.53	19.25	0.90	2.30	6.30	16.07	0.60	2.20	7.30
	DUST3R _{CVPR'24} [90]	5.49	56.45	12.37	1.40	3.80	9.20	13.27	1.40	3.70	8.10
	UniDepth _{CVPR'24} [65]	13.99	204.17	32.16	0.80	1.60	3.00	35.10	0.60	1.50	3.10
	GeoCalib _{ECCV'24} [86]	2.18	19.36	4.91	13.80	30.50	47.80	5.11	13.60	29.60	46.50
	DiffCalib _{AAAI'25} [34]	12.96	178.98	30.28	0.00	0.00	0.00	31.49	0.00	0.00	0.00
	MoGe _{CVPR'25} [89]	0.73	6.24	1.61	26.60	67.00	83.20	1.68	25.40	65.70	82.50
	AnyCalib_{pinhole} (Ours)	1.63	15.02	3.62	15.50	36.40	55.10	3.93	14.70	34.70	53.00
AnyCalib_{gen} (Ours)	1.76	15.98	4.06	13.60	33.40	52.80	4.09	13.90	33.40	52.20	
MegaDepth [49]	Perceptual _{TPAMI'23} [36]	2.54	81.69	6.21	8.80	22.60	39.80	6.52	8.00	20.80	37.60
	WildCam _{NeurIPS'23} [100]	1.65	57.24	2.90	18.60	42.90	63.10	3.42	15.30	37.80	59.30
	DUST3R _{CVPR'24} [90]	0.77	30.75	1.82	31.70	56.70	72.30	1.96	30.00	54.40	70.60
	UniDepth _{CVPR'24} [65]	4.51	128.07	10.82	6.80	16.20	27.40	11.10	5.80	14.90	25.30
	GeoCalib _{ECCV'24} [86]	1.88	57.77	4.56	13.80	31.60	48.10	4.93	13.00	30.20	46.40
	DiffCalib _{AAAI'25} [34]	3.26	113.65	4.26	14.20	31.80	51.30	5.56	9.70	24.40	43.80
	MoGe _{CVPR'25} [89]	1.12	28.58	2.16	25.40	53.50	72.20	2.31	24.50	50.80	69.90
	AnyCalib_{pinhole} (Ours)	1.31	39.51	3.14	19.40	40.80	59.10	3.36	18.00	39.30	57.20
AnyCalib_{gen} (Ours)	1.48	47.11	3.57	14.80	36.60	55.70	3.84	14.90	34.50	53.20	
LaMAR [69]	Perceptual _{TPAMI'23} [36]	2.51	91.78	6.70	7.00	13.90	31.60	5.68	7.00	15.90	36.20
	WildCam _{NeurIPS'23} [100]	1.79	52.30	2.85	18.80	43.90	66.60	2.72	18.80	44.00	64.00
	DUST3R _{CVPR'24} [90]	2.25	84.22	5.99	5.40	17.20	42.00	5.07	6.30	21.40	50.20
	UniDepth _{CVPR'24} [65]	1.14	36.99	2.46	5.10	37.10	49.10	2.89	1.50	32.40	47.90
	GeoCalib _{ECCV'24} [86]	1.17	39.99	3.09	19.00	41.20	59.80	2.65	22.00	45.80	64.00
	DiffCalib _{AAAI'25} [34]	4.18	163.83	11.26	0.00	1.50	15.50	5.34	8.20	22.00	47.40
	MoGe _{CVPR'25} [89]	0.69	25.64	1.97	26.30	55.30	73.50	1.69	31.70	60.60	77.50
	AnyCalib_{pinhole} (Ours)	0.85	28.61	2.25	24.60	51.60	70.50	1.92	28.60	57.10	74.60
AnyCalib_{gen} (Ours)	1.08	35.88	2.81	19.30	44.10	65.00	2.49	21.00	48.30	68.70	

Table 2. **Results on perspective images.** Best and second-best results are highlighted in green and yellow, respectively. Methods trained on evaluated datasets are highlighted in gray and excluded from the ranking to ensure a fair comparison. Among all evaluated methods, only Perceptual [36] and AnyCalib_{gen} are not specifically trained on perspective (pinhole) images. AnyCalib, either trained on perspective-only (AnyCalib_{pin}) or general (AnyCalib_{gen}) projections, performs similarly or better than alternatives, including the 3D foundation models DUST3R [90], UniDepth [65] and MoGe [89], despite AnyCalib is trained on orders of magnitude less data.

method. For [86], we consider its two models, trained with perspective (pin) and radially-distorted (rad) images. We use its implementation of the radial model in MegaDepth [49], and, for the other datasets, we use the division model, since they present strong radial distortions and wider field of views, not appropriate for the radial model [47, 85]. We only evaluate SVA [51] in datasets with strong distortions, as this is an assumption of this method. Note that SVA leads to crashes (lack of estimations) in approximately 38% of

images in both ScanNet++ [95] and Mono [23], as it fails to detect either circular arcs or repeated patterns in the input images, as similarly reported in [36, 86].

Results on Tab. 3 show that AnyCalib, either trained on OP_r (AnyCalib_{radial}), OP_d (AnyCalib_{dist}) or OP_g (AnyCalib_{gen}), is generally more accurate than the alternatives. On ScanNet++ [95], the accuracy of AnyCalib and SVA [52] is comparable. However, AnyCalib is more robust, as SVA leads to crashes in 38% of the images.

Method	AE ↓ [°]	RE ↓ [pix]	vFoV [°]			hFoV [°]					
			error ↓	AUC@1/5/10 ↑		error ↓	AUC@1/5/10 ↑				
MD [49]	Perceptual _{TPAMI'23} [36]	2.63	82.97	6.22	8.40	22.20	39.50	6.88	7.50	20.20	36.60
	GeoCalib-pin _{ECCV'24} [86]	1.97	55.91	4.67	15.00	31.70	47.70	5.03	13.80	30.40	46.10
	GeoCalib-rad _{ECCV'24} [86]	1.93	56.14	4.55	14.20	31.70	47.70	5.01	13.50	30.40	46.20
	AnyCalib_{radial} (Ours)	1.48	45.89	3.63	16.40	36.70	55.90	3.81	14.70	35.00	54.40
	AnyCalib_{gen} (Ours)	1.45	44.63	3.55	15.20	37.10	55.90	3.79	14.00	34.60	53.80
SN++ [95]	SVA _{WACV'21} [51]	2.92	37.64	6.39	21.00	33.80	42.30	6.80	17.60	31.50	41.20
	Perceptual _{TPAMI'23} [36]	3.10	44.08	7.65	0.80	1.70	22.10	3.96	2.60	24.20	39.10
	GeoCalib-pin _{ECCV'24} [86]	7.00	104.72	14.61	1.70	5.40	12.80	20.41	2.00	4.60	10.10
	GeoCalib-rad _{ECCV'24} [86]	4.97	71.07	10.11	3.80	11.30	23.70	14.20	3.40	9.90	18.50
	AnyCalib_{dist} (Ours)	1.59	20.61	3.90	11.20	31.80	57.70	3.38	15.80	39.10	62.60
AnyCalib_{gen} (Ours)	1.88	24.75	4.26	10.50	29.50	55.10	5.05	6.90	23.70	47.50	
Mono [23]	SVA _{WACV'21} [51]	8.29	107.61	19.09	12.20	22.70	31.00	19.64	11.00	21.30	29.80
	Perceptual _{TPAMI'23} [36]	4.06	53.22	9.48	2.10	15.90	26.70	9.09	10.20	14.60	26.60
	GeoCalib-pin _{ECCV'24} [86]	4.38	63.63	10.10	5.00	13.90	26.40	11.73	4.40	12.50	23.40
	GeoCalib-rad _{ECCV'24} [86]	3.94	56.49	7.90	8.40	19.50	33.70	9.47	6.60	16.20	28.80
	AnyCalib_{dist} (Ours)	1.60	21.70	3.60	16.20	37.40	57.30	3.94	15.00	34.20	53.80
AnyCalib_{gen} (Ours)	1.64	22.52	3.66	16.20	36.80	56.20	3.95	14.50	34.20	53.00	

Table 3. **Results on distorted images.** Best and second-best results are highlighted in green and yellow, respectively. AnyCalib, either trained on distorted-only images or general image projections is generally more accurate than alternative methods. Since AnyCalib is model-agnostic, different camera models can be fitted without retraining. To demonstrate this, results in MegaDepth [49], ScanNet++ [95] and Mono [23] use, respectively: the radial (Brown-Conrady) model [14] with one distortion parameter, the Kannala-Brandt model [39] with four distortion parameters and UCM [29, 55] (the model to which Perceptual [36] is tailored). Changing the camera model yields practically the same accuracy, thus providing flexibility in selecting the camera model that best suits a certain application.

Method	Stanford2D3D [7]			TartanAir [91]			LaMAR [69]		
	e_f ↓	e_c ↓	AE [°] ↓	e_f ↓	e_c ↓	AE [°] ↓	e_f ↓	e_c ↓	AE [°] ↓
WildCam _{NeurIPS'23} [100]	0.32	0.47	12.74	0.83	0.38	15.60	0.25	0.51	10.38
DiffCalib _{AAAI'25} [34]	0.40	0.55	14.43	0.62	0.55	18.01	0.24	0.55	11.35
AnyCalib (Ours)	0.15	0.26	7.46	0.19	0.28	9.88	0.22	0.41	9.46

Table 4. **Results on edited (stretched and cropped) images.** Best results are highlighted in green. All evaluated methods estimate the same camera model (pinhole with four degrees of freedom). Compared with the recent WildCam [100] and DiffCalib [34], AnyCalib consistently estimates the focal lengths f_x, f_y , and the arbitrarily placed principal point \mathbf{c} more accurately.

4.3. Edited images

Baselines. We consider WildCam and DiffCalib [34, 100] as they are the only baselines that can deal with edited images.

Metrics. Since both [34, 100] estimate pinhole intrinsics, we follow their evaluation and report median values of relative errors for focal and principal point, defined as: $e_f = \|(\mathbf{f}_{GT} - \mathbf{f})/\mathbf{f}_{GT}\|_\infty$ and $e_c = 2\|(\mathbf{c}_{GT} - \mathbf{c})/[W, H]\|_\infty$, with the division being done elementwise. To compare with previous results we also report the angular error.

Datasets. We consider the same datasets as in Sec. 4.1, excluding MegaDepth, as it already contains crops and [100] is trained on it. Following [34, 100], we randomly resize the images to have pixel-aspect ratios $\in [0.5, 2]$ and randomly crop them to, at most, half of its size.

Results on Tab. 4 confirm that AnyCalib trained on OP_p

with a training strategy based on [34, 100] (Sec. 3.3), also improves over alternative methods on stretched and cropped images. Note that estimating the principal point, arbitrarily placed in the image, is challenging and recognized as an ill-posed problem [19, 72]. This explains the increase in AE.

5. Conclusion

In this paper, we introduced AnyCalib, a novel single-view calibration method that, for the first time, works with edited, perspective and distorted images. We frame the calibration of a camera as the regression of FoV fields, a novel, robust, intermediate representation not tied to extrinsic cues and that is bijective to the pixelwise ray directions of the camera. AnyCalib is model-agnostic, as it calibrates, in closed-form, a wide range of camera models freely chosen at runtime. Experimentally, AnyCalib sets a new state-of-the-art across multiple indoor and outdoor benchmarks.

Acknowledgements

Thanks to Jean-François Lalonde for granting us permission to release our models trained on the Laval Photometric Indoor HDR Dataset. The top row of Fig. 1 uses images from [ExploreCams](#), taken by [Michele Sacchet](#), [srkcalifano](#) and [donchc](#). The input image in Fig. 2 has a [CC BY 2.0 license](#) and its author is [Sergei Gussev](#). This work was supported by the Ministerio de Universidades Scholarship FPU21/04468, the Spanish Government (projects PID2021-127685NB-I00 and TED2021-131150B-I00) and the Aragón Government (project T45_23R).

References

- [1] ambientCG. <https://ambientcg.com/list?type=hdr>. 6
- [2] BlenderKit. https://www.blenderkit.com/asset-gallery?query=category_subtree:hdr. 6
- [3] HDRMAPS. <https://hdrmaps.com/freebies/free-hdris/>. 6
- [4] Lensfun. <https://lensfun.github.io/lenslist/>. 5, 6, 13, 14
- [5] Sameer Agarwal, Yasutaka Furukawa, Noah Snavely, Ian Simon, Brian Curless, Steven M Seitz, and Richard Szeliski. Building Rome in a Day. *Communications of the ACM*, 2011. 2
- [6] Michel Antunes, Joao P. Barreto, Djamilia Aouada, and Bjorn Ottersten. Unsupervised Vanishing Point Detection and Camera Calibration From a Single Manhattan Image With Radial Distortion. In *CVPR*, 2017. 2
- [7] Iro Armeni, Sasha Sax, Amir R Zamir, and Silvio Savarese. Joint 2D-3D-Semantic Data for Indoor Scene Understanding. *arXiv preprint arXiv:1702.01105*, 2017. 6, 7, 8, 18
- [8] Gwangbin Bae and Andrew J. Davison. Rethinking Inductive Biases for Surface Normal Estimation. In *CVPR*, 2024. 2, 13
- [9] Bruno Berenguel-Baeta, Maria Santos-Villafranca, Jesus Bermudez-Cameo, Alejandro Perez Yus, and Josechu Guerrero. Convolution Kernel Adaptation to Calibrated Fisheye. In *BMVC*, 2023. 2
- [10] Oleksandr Bogdan, Viktor Eckstein, Francois Rameau, and Jean-Charles Bazin. DeepCalib: a Deep learning approach for Automatic Intrinsic Calibration of Wide Field-of-View Cameras. In *Proceedings of the 15th ACM SIGGRAPH European Conference on Visual Media Production*, 2018. 2
- [11] Christophe Bolduc, Justine Giroux, Marc Hébert, Claude Demers, and Jean-François Lalonde. Beyond the Pixel: a Photometrically Calibrated HDR Dataset for Luminance and Color Prediction. In *ICCV*, 2023. 6
- [12] Jean-Yves Bouguet. Camera Calibration Toolbox for Matlab. <https://robots.stanford.edu/cs223b04/JeanYvesCalib/>, 2004. 2
- [13] Nicolas Boumal. *An Introduction to Optimization on Smooth Manifolds*. Cambridge University Press, 2023. 3, 4
- [14] Duane C. Brown. Close-Range Camera Calibration. *Photogramm. Eng*, 1971. 5, 6, 8, 13, 14
- [15] Carlos Campos, Richard Elvira, Juan J. Gómez Rodríguez, José M. M. Montiel, and Juan D. Tardós. ORB-SLAM3: An Accurate Open-Source Library for Visual, Visual-Inertial, and Multimap SLAM. *IEEE T-RO*, 2021. 2
- [16] Yisong Chen, Horace Ip, Zhangjin Huang, and Guoping Wang. Full Camera Calibration from a Single View of Planar Scene. In *Advances in Visual Computing: 4th International Symposium, ISVC 2008*, 2008. 2
- [17] Javier Civera, Diana R. Bueno, Andrew J. Davison, and José María M. Montiel. Camera Self-Calibration for Sequential Bayesian Structure from Motion. In *IEEE ICRA*, 2009. 2
- [18] Andrea Porfiri Dal Cin, Francesco Azzoni, Giacomo Boracchi, and Luca Magri. Revisiting Calibration of Wide-Angle Radially Symmetric Cameras. In *ECCV*, 2024. 3, 6
- [19] Lourdes de Agapito, Eric Hayman, and Ian Reid. Self-Calibration of a Rotating Camera with Varying Intrinsic Parameters. In *BMVC*, 1998. 5, 8
- [20] Frank Dellaert and Michael Kaess. *Factor Graphs for Robot Perception*. Foundations and Trends in Robotics, Vol. 6, 2017. 3
- [21] Jonathan Deutscher, Michael Isard, and John MacCormick. Automatic Camera Calibration from a Single Manhattan Image. In *ECCV*, 2002. 2
- [22] Alexey Dosovitskiy, Lucas Beyer, Alexander Kolesnikov, Dirk Weissenborn, Xiaohua Zhai, Thomas Unterthiner, Mostafa Dehghani, Matthias Minderer, Georg Heigold, Sylvain Gelly, Jakob Uszkoreit, and Neil Houlsby. An Image is Worth 16x16 Words: Transformers for Image Recognition at Scale. In *ICLR*, 2021. 5
- [23] Jakob Engel, Vladyslav Usenko, and Daniel Cremers. A Photometrically Calibrated Benchmark For Monocular Visual Odometry. *arXiv:1607.02555*, 2016. 6, 7, 8, 22, 24
- [24] Jose M. Facil, Benjamin Ummenhofer, Huizhong Zhou, Luis Montesano, Thomas Brox, and Javier Civera. CAM-ConvS: Camera-Aware Multi-Scale Convolutions for Single-View Depth. In *CVPR*, 2019. 2
- [25] Martin A. Fischler and Robert C. Bolles. Random Sample Consensus: A Paradigm for Model Fitting with Applications to Image Analysis and Automated Cartography. *Communications of the ACM*, 1981. 13
- [26] Andrew W. Fitzgibbon. Simultaneous Linear Estimation of Multiple View Geometry and Lens Distortion. In *CVPR*, 2001. 5
- [27] Paul Furgale, Joern Rehder, and Roland Siegwart. Unified Temporal and Spatial Calibration for Multi-Sensor Systems. In *IEEE/RSJ IROS*, 2013. 2
- [28] Marc-André Gardner, Kalyan Sunkavalli, Ersin Yumer, Xiaohui Shen, Emiliano Gambaretto, Christian Gagné, and Jean-François Lalonde. Learning to Predict Indoor Illumination from a Single Image. *ACM SIGGRAPH Asia*, 2017. 6
- [29] Christopher Geyer and Kostas Daniilidis. A Unifying Theory for Central Panoramic Systems and Practical Implications. In *ECCV*, 2000. 5, 8
- [30] Rafael Grompone von Gioi, Jeremie Jakubowicz, Jean-Michel Morel, and Gregory Randall. LSD: A Fast Line

- Segment Detector with a False Detection Control. *IEEE TPAMI*, 2010. 2
- [31] Michael D. Grossberg and Shree K. Nayar. A General Imaging Model and a Method for Finding its Parameters. In *ICCV*, 2001. 2
- [32] Annika Hagemann, Moritz Knorr, and Christoph Stiller. Deep Geometry-Aware Camera Self-Calibration from Video. In *ICCV*, 2023. 2
- [33] Richard I. Hartley and Andrew Zisserman. *Multiple View Geometry in Computer Vision*. Cambridge University Press, ISBN: 0521540518, second edition, 2004. 2, 16
- [34] Xiankang He, Guangkai Xu, Bo Zhang, Hao Chen, Ying Cui, and Dongyan Guo. DiffCalib: Reformulating Monocular Camera Calibration as Diffusion-Based Dense Incident Map Generation. In *AAAI*, 2025. 3, 5, 6, 7, 8, 16, 23
- [35] Yannick Hold-Geoffroy, Kalyan Sunkavalli, Jonathan Eisenmann, Matthew Fisher, Emiliano Gambaretto, Sunil Hadap, and Jean-François Lalonde. A Perceptual Measure for Deep Single Image Camera Calibration. In *CVPR*, 2018. 2
- [36] Yannick Hold-Geoffroy, Dominique Piché-Meunier, Kalyan Sunkavalli, Jean-Charles Bazin, François Rameau, and Jean-François Lalonde. A Perceptual Measure for Deep Single Image Camera and Lens Calibration. *IEEE TPAMI*, 2023. 2, 3, 6, 7, 8
- [37] Mu Hu, Wei Yin, Chi Zhang, Zhipeng Cai, Xiaoxiao Long, Hao Chen, Kaixuan Wang, Gang Yu, Chunhua Shen, and Shaojie Shen. Metric3D v2: A Versatile Monocular Geometric Foundation Model for Zero-Shot Metric Depth and Surface Normal Estimation. *IEEE TPAMI*, 2024. 2
- [38] Linyi Jin, Jianming Zhang, Yannick Hold-Geoffroy, Oliver Wang, Kevin Blackburn-Matzen, Matthew Sticha, and David F. Fouhey. Perspective Fields for Single Image Camera Calibration. In *CVPR*, 2023. 2, 3, 4, 6
- [39] Juho Kannala and Sami S. Brandt. A Generic Camera Model and Calibration Method for Conventional, Wide-Angle, and Fish-eye Lenses. *IEEE TPAMI*, 2006. 5, 8, 13, 14, 15, 16
- [40] Bernhard Kerbl, Georgios Kopanas, Thomas Leimkuehler, and George Drettakis. 3D Gaussian Splatting for Real-Time Radiance Field Rendering. *ACM Trans. Graph.*, 2023. 2
- [41] Bogdan Khomutenko, Gaëtan Garcia, and Philippe Martinet. An Enhanced Unified Camera Model. *IEEE RA-L*, 2016. 5, 6, 13, 14
- [42] Florian Kluger, Eric Brachmann, Hanno Ackermann, Carsten Rother, Michael Ying Yang, and Bodo Rosenhahn. CONSAC: Robust Multi-Model Fitting by Conditional Sample Consensus. In *CVPR*, 2020. 2
- [43] Muhammed Kocabas, Chun-Hao P. Huang, Joachim Tesch, Lea Müller, Otmar Hilliges, and Michael J. Black. SPEC: Seeing People in the Wild With an Estimated Camera. In *ICCV*, 2021. 3
- [44] Jana Košecká and Wei Zhang. Video Compass. In *ECCV*, 2002. 2
- [45] Viktor Larsson, Torsten Sattler, Zuzana Kukelova, and Marc Pollefeys. Revisiting Radial Distortion Absolute Pose. In *ICCV*, 2019. 5
- [46] Jinwoo Lee, Hyunsung Go, Hyunjoon Lee, Sunghyun Cho, Minhyuk Sung, and Junho Kim. CTRL-C: Camera Calibration TRansformer With Line-Classification. In *ICCV*, 2021. 2, 3
- [47] Matthew J. Leotta, David Russell, and Andrew Matrai. On the Maximum Radius of Polynomial Lens Distortion. In *WACV*, 2022. 6, 7, 13, 14
- [48] Xiaoyu Li, Bo Zhang, Pedro V. Sander, and Jing Liao. Blind Geometric Distortion Correction on Images Through Deep Learning. In *CVPR*, 2019. 3
- [49] Zhengqi Li and Noah Snavely. MegaDepth: Learning Single-View Depth Prediction From Internet Photos. In *CVPR*, 2018. 2, 6, 7, 8, 20
- [50] Daniel Lichy, Hang Su, Abhishek Badki, Jan Kautz, and Orazio Gallo. FoVA-Depth: Field-of-View Agnostic Depth Estimation for Cross-Dataset Generalization. In *3DV*, 2024. 2
- [51] Yaroslava Lochman, Oles Doboševych, Rostyslav Hryniv, and James Pritts. Minimal Solvers for Single-View Lens-Distorted Camera Auto-Calibration. In *WACV*, 2021. 2, 6, 7, 8
- [52] Yaroslava Lochman, Kostiantyn Liepieshov, Jianhui Chen, Michal Perdoch, Christopher Zach, and James Pritts. BabelCalib: A Universal Approach to Calibrating Central Cameras. In *ICCV*, 2021. 2, 4, 5, 6, 7, 15, 16
- [53] Manuel Lopez, Roger Mari, Pau Gargallo, Yubin Kuang, Javier Gonzalez-Jimenez, and Gloria Haro. Deep Single Image Camera Calibration With Radial Distortion. In *CVPR*, 2019. 2, 3
- [54] Ilya Loshchilov and Frank Hutter. Decoupled Weight Decay Regularization. In *ICLR*, 2019. 5
- [55] Christopher Mei and Patrick Rives. Single View Point Omnidirectional Camera Calibration from Planar Grids. In *IEEE ICRA*, 2007. 5, 6, 8, 15
- [56] Ben Mildenhall, Pratul P. Srinivasan, Matthew Tancik, Jonathan T. Barron, Ravi Ramamoorthi, and Ren Ng. NeRF: Representing Scenes as Neural Radiance Fields for View Synthesis. In *ECCV*, 2020. 2
- [57] Raúl Mur-Artal and Juan D. Tardós. ORB-SLAM2: An Open-Source SLAM System for Monocular, Stereo, and RGB-D Cameras. *IEEE T-RO*, 2017. 2
- [58] Raul Mur-Artal, Jose Maria Martinez Montiel, and Juan D Tardos. ORB-SLAM: A Versatile and Accurate Monocular SLAM System. *IEEE T-RO*, 2015. 2
- [59] Riku Murai, Eric Dexheimer, and Andrew J. Davison. MAST3R-SLAM: Real-Time Dense SLAM with 3D Reconstruction Priors. *arXiv preprint arXiv:2412.12392*, 2024. 2
- [60] Maxime Oquab, Timothée Darcet, Théo Moutakanni, Huy V. Vo, Marc Szafraniec, Vasil Khalidov, Pierre Fernandez, Daniel HAZIZA, Francisco Massa, Alaaeldin El-Nouby, Mido Assran, Nicolas Ballas, Wojciech Galuba, Russell Howes, Po-Yao Huang, Shang-Wen Li, Ishan Misra, Michael Rabbat, Vasu Sharma, Gabriel Synnaeve, Hu Xu, Herve Jegou, Julien Mairal, Patrick Labatut, Armand Joulin, and Piotr Bojanowski. DINOv2: Learning Robust Visual Features without Supervision. *TMLR*, 2024. 5

- [61] Linfei Pan, Dániel Baráth, Marc Pollefeys, and Johannes L Schönberger. Global Structure-from-Motion Revisited. In *ECCV*, 2024. 2
- [62] Priyanka Patel and Michael J Black. CameraHMR: Aligning People with Perspective. In *3DV*, 2025. 3
- [63] Rémi Pautrat, Daniel Barath, Viktor Larsson, Martin R. Oswald, and Marc Pollefeys. DeepLSD: Line Segment Detection and Refinement With Deep Image Gradients. In *CVPR*, 2023. 2
- [64] Rémi Pautrat, Shaohui Liu, Petr Hruby, Marc Pollefeys, and Daniel Barath. Vanishing Point Estimation in Uncalibrated Images with Prior Gravity Direction. In *ICCV*, 2023. 2
- [65] Luigi Piccinelli, Yung-Hsu Yang, Christos Sakaridis, Matia Segu, Siyuan Li, Luc Van Gool, and Fisher Yu. UniDepth: Universal Monocular Metric Depth Estimation. In *CVPR*, 2024. 6, 7
- [66] James Pritts, Zuzana Kukelova, Viktor Larsson, and Ondřej Chum. Radially-Distorted Conjugate Translations. In *CVPR*, 2018. 2
- [67] René Ranftl, Alexey Bochkovskiy, and Vladlen Koltun. Vision Transformers for Dense Prediction. In *ICCV*, 2021. 2, 5, 13
- [68] Nikon Rumors. Nikkor 6mm f/2.8 fisheye lens video and photo samples. <https://nikonrumors.com/2014/11/25/nikkor-6mm-f2-8-fisheye-lens-video-and-photo-samples.aspx/>. 5
- [69] Paul-Edouard Sarlin, Mihai Dusmanu, Johannes L. Schönberger, Pablo Speciale, Lukas Gruber, Viktor Larsson, Ondrej Miksik, and Marc Pollefeys. LaMAR: Benchmarking Localization and Mapping for Augmented Reality. In *ECCV*, 2022. 6, 7, 8, 19
- [70] Davide Scaramuzza, Agostino Martinelli, and Roland Siegwart. A Flexible Technique for Accurate Omnidirectional Camera Calibration and Structure from Motion. In *IEEE ICVS*, 2006. 5
- [71] Davide Scaramuzza, Agostino Martinelli, and Roland Siegwart. A Toolbox for Easily Calibrating Omnidirectional Cameras. In *IEEE/RSJ IROS*, 2006. 2
- [72] Johannes L. Schönberger and Jan-Michael Frahm. Structure-From-Motion Revisited. In *CVPR*, 2016. 2, 5, 8
- [73] Thomas Schops, Viktor Larsson, Marc Pollefeys, and Torsten Sattler. Why Having 10,000 Parameters in Your Camera Model Is Better Than Twelve. In *CVPR*, 2020. 2
- [74] Movie Camera Shots. Dolly Zoom Shot - E.T. The Extra-Terrestrial (1982). <https://youtu.be/ZABX9cf3KSY>. 4
- [75] Xu Song, Hao Kang, Atsunori Moteki, Genta Suzuki, Yoshie Kobayashi, and Zhiming Tan. MSCC: Multi-Scale Transformers for Camera Calibration. In *WACV*, 2024. 2
- [76] Philip B. Stark and Robert L. Parker. Bounded-Variable Least-Squares: an Algorithm and Applications. *Computational Statistics*, 1995. 5
- [77] Eric Stemen. Dolly Zoom Tutorial for Timelapse Hyperlapse. <https://youtu.be/Azo5HfgHrro>. 4
- [78] Rainer Storn and Kenneth Price. Differential Evolution—A Simple and Efficient Heuristic for Global Optimization over Continuous Spaces. *Journal of global optimization*, 1997. 3
- [79] Sebastian Janampa Student and Marios Pattichis. SOFI: Multi-Scale Deformable Transformer for Camera Calibration with Enhanced Line Queries. In *BMVC*, 2024. 2
- [80] Peter Sturm, Srikumar Ramalingam, Jean-Philippe Tardif, Simone Gasparini, Joao Barreto, et al. Camera Models and Fundamental Concepts Used in Geometric Computer Vision. *Foundations and Trends® in Computer Graphics and Vision*, 2011. 2
- [81] Zachary Teed and Jia Deng. RAFT: Recurrent All-Pairs Field Transforms for Optical Flow. In *ECCV*, 2020. 5
- [82] Zachary Teed and Jia Deng. RAFT-3D: Scene Flow Using Rigid-Motion Embeddings. In *CVPR*, 2021. 3
- [83] Bill Triggs, Philip F. McLauchlan, Richard I. Hartley, and Andrew W. Fitzgibbon. Bundle Adjustment — A Modern Synthesis. In *Vision Algorithms: Theory and Practice*, 2000. 5
- [84] Steffen Urban, Jens Leitloff, and Stefan Hinz. Improved Wide-Angle, Fisheye and Omnidirectional Camera Calibration. *ISPRS JPRS*, 2015. 2, 5
- [85] Vladyslav Usenko, Nikolaus Demmel, and Daniel Cremers. The Double Sphere Camera Model. In *3DV*, 2018. 2, 3, 4, 5, 6, 7, 13, 14, 16
- [86] Alexander Veicht, Paul-Edouard Sarlin, Philipp Lindenberger, and Marc Pollefeys. GeoCalib: Single-image Calibration with Geometric Optimization. In *ECCV*, 2024. 2, 3, 4, 5, 6, 7, 8, 13, 14
- [87] Nobuhiko Wakai, Satoshi Sato, Yasunori Ishii, and Takayoshi Yamashita. Rethinking Generic Camera Models for Deep Single Image Camera Calibration to Recover Rotation and Fisheye Distortion. In *ECCV*, 2022. 2
- [88] Nobuhiko Wakai, Satoshi Sato, Yasunori Ishii, and Takayoshi Yamashita. Deep Single Image Camera Calibration by Heatmap Regression to Recover Fisheye Images Under Manhattan World Assumption. In *CVPR*, 2024. 2
- [89] Ruicheng Wang, Sicheng Xu, Cassie Dai, Jianfeng Xiang, Yu Deng, Xin Tong, and Jiaolong Yang. MoGe: Unlocking Accurate Monocular Geometry Estimation for Open-Domain Images with Optimal Training Supervision. In *CVPR*, 2025. 6, 7
- [90] Shuzhe Wang, Vincent Leroy, Yohann Cabon, Boris Chidlovskii, and Jerome Revaud. DUST3R: Geometric 3D Vision Made Easy. In *CVPR*, 2024. 6, 7
- [91] Wenshan Wang, DeLong Zhu, Xiangwei Wang, Yaoyu Hu, Yuheng Qiu, Chen Wang, Yafei Hu, Ashish Kapoor, and Sebastian Scherer. TartanAir: A Dataset to Push the Limits of Visual SLAM. In *IEEE/RSJ IROS*, 2020. 6, 7, 8, 17
- [92] Horst Wildenauer and Allan Hanbury. Robust Camera Self-Calibration from Monocular Images of Manhattan Worlds. In *CVPR*, 2012. 2
- [93] Horst Wildenauer and Branislav Micusik. Closed Form Solution for Radial Distortion Estimation from a Single Vanishing Point. In *BMVC*, 2013. 2
- [94] Wenqi Xian, Zhengqi Li, Matthew Fisher, Jonathan Eisenmann, Eli Shechtman, and Noah Snavely. UprightNet: Geometry-Aware Camera Orientation Estimation From Single Images. In *ICCV*, 2019. 3

- [95] Chandan Yeshwanth, Yueh-Cheng Liu, Matthias Nießner, and Angela Dai. ScanNet++: A High-Fidelity Dataset of 3D Indoor Scenes. In *ICCV*, 2023. 6, 7, 8, 14, 15, 21, 24
- [96] Wei Yin, Chi Zhang, Hao Chen, Zhipeng Cai, Gang Yu, Kaixuan Wang, Xiaozhi Chen, and Chunhua Shen. Metric3D: Towards Zero-shot Metric 3D Prediction from A Single Image. In *ICCV*, 2023. 2
- [97] Senthil Yogamani, Ciaran Hughes, Jonathan Horgan, Ganesh Sistu, Padraig Varley, Derek O’Dea, Michal Uricar, Stefan Milz, Martin Simon, Karl Amende, Christian Witt, Hazem Rashed, Sumanth Chennupati, Sanjaya Nayak, Saquib Mansoor, Xavier Perrotton, and Patrick Perez. WoodScape: A Multi-Task, Multi-Camera Fisheye Dataset for Autonomous Driving. In *ICCV*, 2019. 5
- [98] Greg Zaal, Sergej Majboroda, and Dimitrios Savva. Poly Haven. <https://polyhaven.com/hdris>. 4, 6
- [99] Zhengyou Zhang. A Flexible New Technique for Camera Calibration. *IEEE TPAMI*, 2000. 2
- [100] Shengjie Zhu, Abhinav Kumar, Masa Hu, and Xiaoming Liu. Tame a Wild Camera: In-the-Wild Monocular Camera Calibration. In *NeurIPS*, 2023. 2, 3, 5, 6, 7, 8, 13, 16, 23

AnyCalib: On-Manifold Learning for Model-Agnostic Single-View Camera Calibration

Supplementary Material

A. Ablations

We report ablation results in Tab. 5. Experiments 1-4. are conducted by training AnyCalib on OP_p and averaging errors across the benchmarks of Sec. 4.1. The fifth, RANSAC, ablation, is performed on ScanNet++, following Sec. 4.2. MACs are computed for a 280×364 input image, which results from resizing an image with a 3:4 ($H:W$) aspect ratio to the training resolution of 320^2 pixels.

1-2. Intermediate representation. We test the performance of AnyCalib when learning rays instead of our proposed FoV fields (Sec. 3.1). As first baseline, we use the target representation (rays) and loss function of WildCam [100], which is a cosine similarity loss. As a stronger baseline, we evaluate also the training strategy of DSINE [8] for learning rays *i.e.* using an angular loss. Compared to these baselines, FoV fields lead to more accurate calibrations.

3. Decoder architecture. Our proposed light DPT decoder, when compared to the original [67], decreases $\sim 20\%$ the computation and leads to slight accuracy improvements.

4. Dataset extension. Our extended version of OpenPano [86] leads to improved accuracy. This experiment shows that AnyCalib is scalable.

5. RANSAC [25] can also be applied to our derivations in Sec. 3.2 by using minimal samples from the set of 2D-3D correspondences between the regressed rays and image points. However, minimal samples lead to inaccurate intrinsics when fitting high-complexity camera models such as Kannala-Brandt (KB) [39]. This motivates our non-minimal estimation of the intrinsics.

In conclusion, FoV fields are an appropriate intermediate representation for calibration and key to the performance of AnyCalib: their supervision, when compared to alternatives, leads to learning patterns that are more useful. Moreover, since FoV fields are not tied to extrinsic cues, this is what has allowed us to extend the training dataset with panoramas not aligned with the gravity direction.

B. Datasets details

As mentioned in Sec. 3.3, we create four datasets. We separately train AnyCalib in each of them to study its accuracy according to the trained projection models. The intrinsics used to create the datasets are detailed in Tab. 6. For the camera rotations⁷ we follow GeoCalib [86] and uniformly

⁷For panoramas not aligned with the gravity direction, these rotations are only approximate.

Experiment	RE	{v, h}FoV		MACs
AnyCalib	23.81	2.89	3.02	187.8G
1. Learning rays as [100]	26.05	3.13	3.24	187.8G
2. Learning rays as [8]	24.95	3.02	3.13	187.8G
3. Original DPT [67]	24.99	3.00	3.12	243.2G
4. Orig. OpenPano [86]	26.62	3.23	3.35	187.8G
AnyCalib	20.61	3.90	3.38	n/a
5. RANSAC in KB [39]	1019	16.1	16.2	n/a

Table 5. **Ablation study** over representation, decoder design, dataset and intrinsics fitting method. See Supp. A for details.

sample the roll and pitch angles within $\pm 45^\circ$. All datasets are formed by sampling 16 square images in each of the 3651/202/202 training/val/test panoramas, which yields an approximate distribution of 54k/3k/3k training/val/test images per dataset.

Obtaining the focal length. As shown in Tab. 6, we do not directly sample the focal length f . Instead, to ensure a uniform distribution of image FoVs, we indirectly sample it from the rest of the parameters. For pinhole images, we use the well-known conversion $f = (H/2)/\tan(\text{FoV}/2)$. For BC [14] and EUCM [41], we note that, from Eq. (8):

$$f = \frac{H/2}{R \phi(R, Z)}, \quad \begin{matrix} R = \sin(\text{FoV}/2), \\ Z = \cos(\text{FoV}/2), \end{matrix} \quad (13)$$

since we form the datasets with square images ($H = W$), unit aspect ratio and centered principal point. During training, images are geometrically transformed on-the-fly to match the training resolution and sampled aspect-ratio.

Ensuring valid intrinsics. Independently sampling intrinsics of BC [14] and EUCM [41] can lead to projection models that project different, distant, rays to the same image coordinates [47], which is not physically valid. We guard for this by clamping f according to its limits [47, 85]:

$$\text{BC} \rightarrow f \geq \begin{cases} 0 & \text{if } k \geq 0, \\ \frac{r_{\text{im}}}{r_{\text{max}}(1+kr_{\text{max}}^2)} & \text{if } k < 0, \end{cases} \quad (14)$$

$$\text{EUCM} \rightarrow f \geq \begin{cases} 0 & \text{if } \alpha \leq 0.5, \\ r_{\text{im}}\sqrt{\beta(2\alpha-1)} & \text{if } \alpha > 0.5, \end{cases} \quad (15)$$

where $r_{\text{im}} = 0.5(H^2 + W^2)^{0.5}$ and $r_{\text{max}} = 1/\sqrt{-3k}$.

Mapping LensFun coefficients. As explained in Sec. 3.3 and Fig. 4, we use the LensFun database [4] for defining the sampling bounds of EUCM’s α and β . LensFun uses

Data	Models	FoV [°]	$\hat{k} = kH/f$	α	β
OP _p	100% pinhole	$\mathcal{U}(20, 105)$	-	-	-
OP _r	100% BC [14]	$\mathcal{U}(20, 105)$	$\mathcal{N}_t(0, 0.07, [-0.3, 0.3])$	-	-
OP _d	50% BC [14]	$\mathcal{U}(20, 105)$	$\mathcal{N}_t(0, 0.07, [-0.3, 0.3])$	-	-
	50% EUCM [41]	$\mathcal{U}(50, 180)$	-	$\mathcal{U}(0.5, 0.8)$	$\mathcal{U}(0.5, 2)$
OP _g	34% pinhole	$\mathcal{U}(20, 105)$	-	-	-
	33% BC [14]	$\mathcal{U}(20, 105)$	$\mathcal{N}_t(0, 0.07, [-0.3, 0.3])$	-	-
	33% EUCM [41]	$\mathcal{U}(50, 180)$	-	$\mathcal{U}(0.5, 0.8)$	$\mathcal{U}(0.5, 2)$

Table 6. **Sampling distributions within the datasets.** $\mathcal{U}(a, b)$ denotes a uniform distribution $\in [a, b]$. $\mathcal{N}_t(\mu, \sigma, [a, b])$ denotes a normal distribution $\mathcal{N}(\mu, \sigma)$ truncated at $[a, b]$. **OP_p** and **OP_r** follow the setup of GeoCalib [86]. Since the distortions allowed by the Brown-Conrady (radial) model [14] are limited [47, 85], for creating **OP_d** and **OP_g**, we use EUCM [41] to generate strongly distorted images. The limits for sampling its parameters α and β are based on real-lens values from the public LensFun database [4] (Fig. 4).

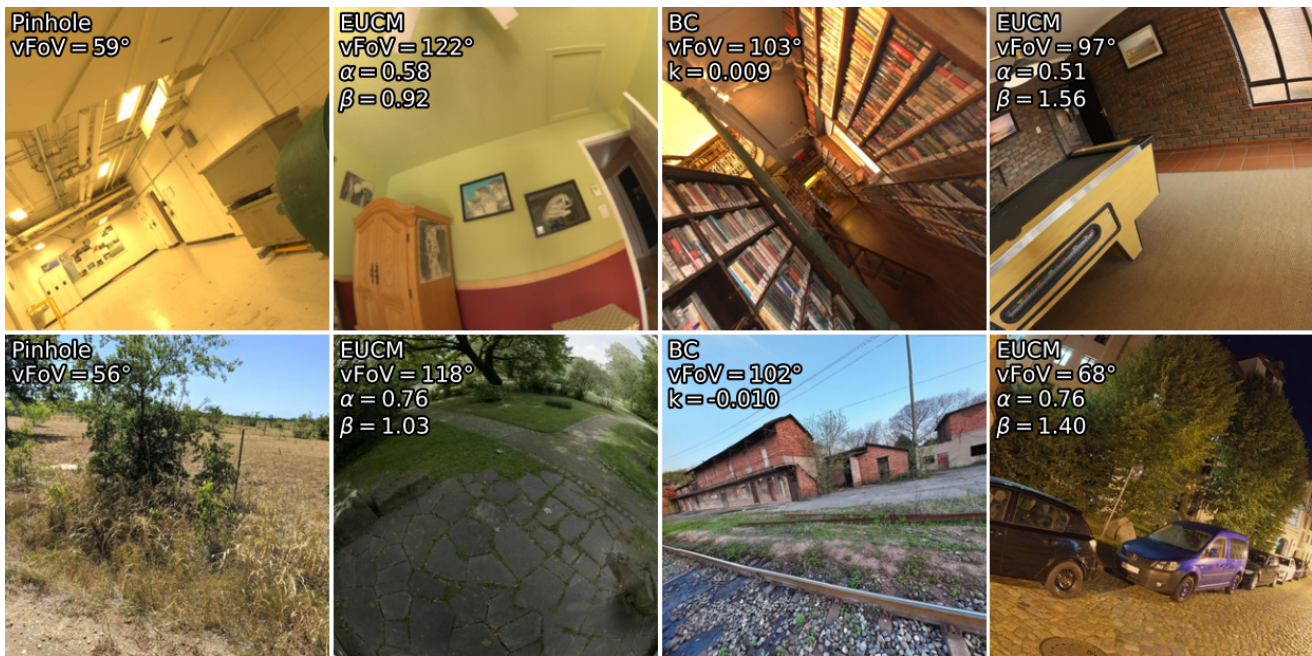


Figure 5. **Sample** images and intrinsics from the dataset OP_g.

its own polynomial distortion models⁸, so we need to map them. Conveniently, our formulation in Sec. 3.2 is applicable: given normalized image coordinates (obtained with the lens focal and image sensor size) and their unprojected rays, we can linearly recover α and β . For getting these unprojections, we first undistort a uniform grid of image/sensor coordinates using Newton’s root finding algorithm and finally invert the ideal (equisolid, equidistant, orthographic or stereographic [4]) fisheye projection model of the lens.

Sample datapoints of OP_g are shown in Fig. 5.

⁸Explained in https://lensfun.github.io/manual/v0.3.2/group__Lens.html#gaa505e04666a189274ba66316697e308e

C. Model-agnostic evaluation

Intrinsics in different models. Different camera models, can have an order of magnitude difference in their focal length f values [85, Tab. 3]. We visualize this behavior in Fig. 6 by mapping the ground-truth Kannala-Brandt (KB) [39] intrinsics from ScanNet++ [95] to UCM intrinsics using our formulation from Sec. 3.2. As shown, if we fix the ground-truth KB focal length and only map the distortion coefficients, the resulting UCM intrinsics fail to accurately model the camera lens projection, leading to an undistortion failure. The converse occurs when we also map the focal length.

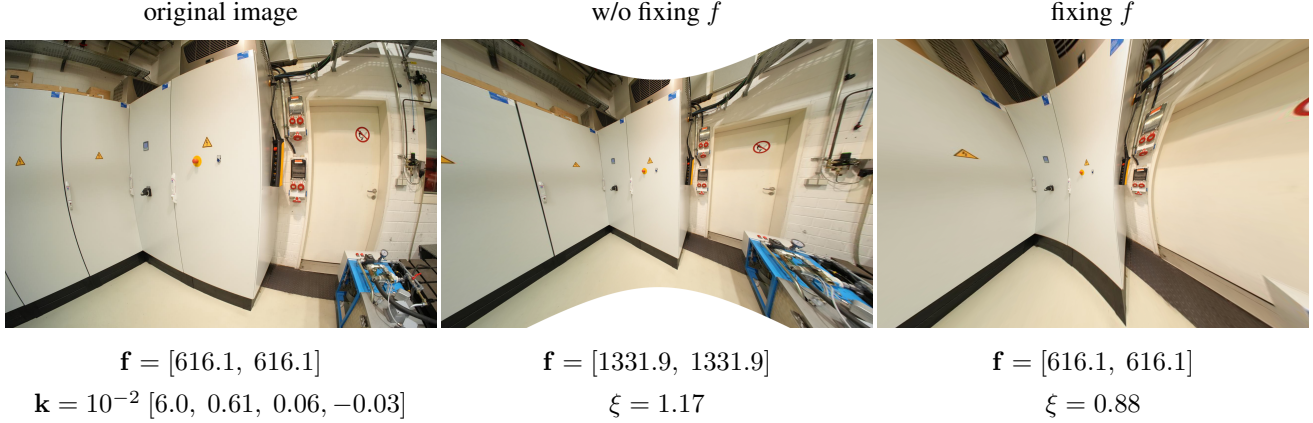
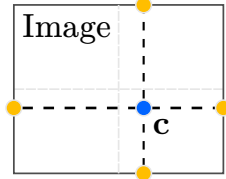


Figure 6. **The focal length (f) in different camera models** can take significantly different values. We show this for UCM [55]. We map the KB [39] intrinsics corresponding to an image from ScanNet++ [95] (left) to UCM following Sec. 3.2. We do this without fixing f , *i.e.*, also mapping it to UCM (middle) and fixing it (right). The resulting intrinsics are used to undistort the image. The same KB focal for UCM leads to a model that does not truthfully model the lens, leading to a failed undistortion. The converse occurs when also mapping f .

Model-agnostic FoV. The horizontal (hFoV) and vertical (vFoV) angular extents of an image can be computed independently of the camera model. To compute the hFoV, we unproject the rays located at the left and right borders, based on the location of the principal point, \mathbf{c} (yellow points on the schematic on the right), and sum the angles between them and the optical axis. The vFoV is computed similarly, but using the top and bottom borders instead.



D. Linear constraints

Lochman et al. [52] show that the distortion parameters of a wide range of camera models can be estimated linearly from 1D-1D correspondences between the radii on the retinal plane, $\|(\mathbf{x} - \mathbf{c})/f\|$, and the ray radii, $\sqrt{X^2 + Y^2}$. Building on this, we show in this section that, together with Eq. (11), *all the intrinsics* of a wide range of standard camera models can be linearly recovered from 2D-3D correspondences between image coordinates $\mathbf{x} \in \Omega$ and ray directions in \mathcal{S}^2 .

To obtain the remaining linear constraints, presented in Tab. 1, we first define auxiliary variables according to the notation in Sec. 3.2:

$$R_a := \sqrt{X^2 + a^2 Y^2}, \quad r_c := \|\mathbf{x} - \mathbf{c}\|, \quad (16)$$

$$\theta := \text{atan2}(R, Z), \quad r := \sqrt{m_x^2 + m_y^2}, \quad (17)$$

$$d := \sqrt{R^2 + Z^2}, \quad r_{ca}^2 := (u - c_x)^2 + (v - c_y)^2 / a^2. \quad (18)$$

For forward camera models (Eq. (8)), the linear constraints

derive from Eq. (21):

$$\pi(\mathbf{p}) = \mathbf{x} = f \phi(R, Z) \begin{bmatrix} X \\ aY \end{bmatrix} + \mathbf{c}, \quad (19)$$

$$\implies \|\mathbf{x} - \mathbf{c}\| = f \phi(R, Z) \left\| \begin{bmatrix} X \\ aY \end{bmatrix} \right\|, \quad (20)$$

$$\implies r_c = f \phi(R, Z) R_a. \quad (21)$$

by substituting the corresponding model-specific function $\phi(R, Z)$ from Tab. 1.

Pinhole: $r_c = \frac{f}{Z} R_a \implies R_a f = Z r_c.$

Brown-Conrady:

$$r_c = f \frac{R_a}{Z} \left(1 + \sum_{n=1}^N k_n (R/Z)^{2n} \right), \quad (22)$$

$$\implies r_c Z / f - R_a \sum_{n=1}^N k_n (R/Z)^{2n} = R_a. \quad (23)$$

Kannala-Brandt:

$$r_c = f \frac{R_a}{R} \left(\theta + \sum_{n=1}^N k_n \theta^{2n+1} \right), \quad (24)$$

$$\implies R r_c / f - R_a \sum_{n=1}^N k_n \theta^{2n+1} = R_a \theta. \quad (25)$$

UCM:

$$r_c = f \frac{R_a}{\xi d + Z} \implies R_a f - r_c d \xi = r_c Z. \quad (26)$$

EUCM For this camera model, linearity in Eq. (21) is lost when f is unknown. Instead, to estimate f , we use a proxy

camera model [39] that leads to practically the same focal length value [52, 85]. Thus, instead of Eq. (10) we start from $r = \phi(R, Z)R$, which for the EUCM model, leads to:

$$r = \frac{R}{\alpha\sqrt{\beta R^2 + Z^2} + (1 - \alpha)Z}, \quad (27)$$

$$\implies r\alpha\sqrt{\beta R^2 + Z^2} = R - (1 - \alpha)Zr, \quad (28)$$

$$\implies r^2\alpha^2(\beta R^2 + Z^2) = (R^2 - (1 - \alpha)Zr)^2, \quad (29)$$

$$\implies r^2R^2\alpha^2\beta + 2rZ(rZ - R)\alpha = (R - rZ)^2. \quad (30)$$

Division For this backward model, from Eq. (9) we know that

$$f \begin{bmatrix} X \\ Y \\ Z \end{bmatrix} = \lambda \begin{bmatrix} (u - c_x) \\ (v - c_y)/a \\ f\psi(r) \end{bmatrix}. \quad (31)$$

To remove the nonlinearity stemming from λ , we use an approach similar to DLT [33]. Since both sides must be parallel, their cross product is the null vector, which leads to the following constraints:

$$(f + \sum_{n=1}^N k'_n r_{ca}^{2n}) \begin{bmatrix} X \\ aY \end{bmatrix} = Z(\mathbf{x} - \mathbf{c}), \quad (32)$$

with $k'_n := k_n/f^{2n-1}$. As inferred from Eq. (31), these two equations are linearly dependent. Thus, we consider only the norm of both sides, which results in:

$$R_a(f + \sum_{n=1}^N k'_n r_{ca}^{2n}) = Zr_c. \quad (33)$$

E. Additional qualitative results

We show qualitative results, using AnyCalib_{gen} (trained on OP_g) on perspective images in Figs. 7 to 10 and on distorted images in Figs. 11 and 12. We also show undistortion results using the same model in Fig. 14. Additional qualitative results on edited (stretched and cropped) images are shown in Fig. 13, with AnyCalib being trained following [34, 100] (Sec. 3.3).

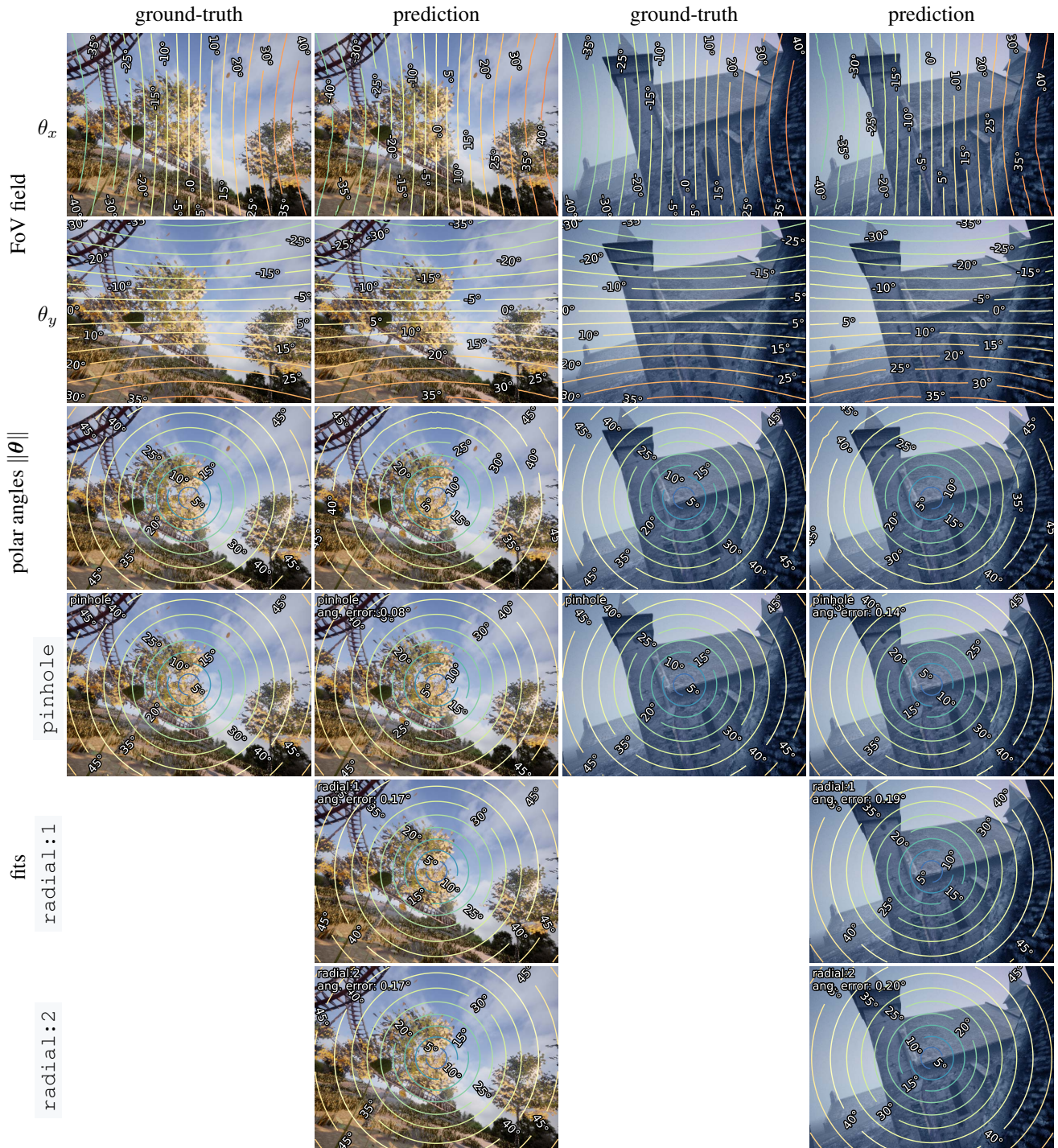


Figure 7. **Qualitative results on perspective images** in TartanAir [91] with AnyCalib_{gen}—trained on OP_g. The FoV field (θ_x and θ_y) is regressed by the network and $\|\theta\|$ represents both its norm and the polar angle of the ray corresponding to each pixel. The predicted FoV field is used to fit the camera model of choice. `radial:i` corresponds to the Brown-Conrady model with `i` distortion coefficients.

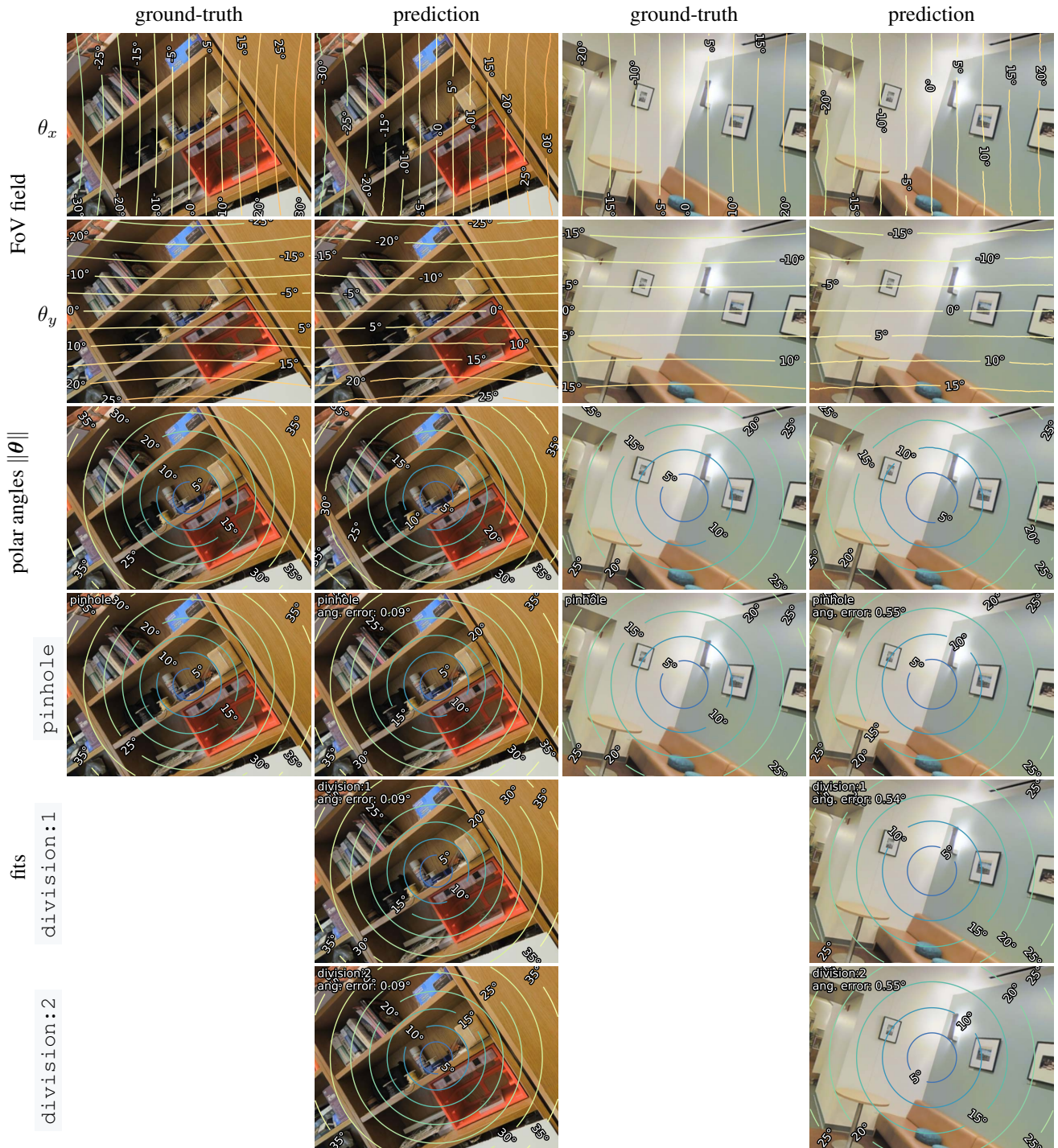


Figure 8. **Qualitative results on perspective images** in Stanford2D3D [7] with AnyCalib_{gen}—trained on OP_g. The FoV field (θ_x and θ_y) is regressed by the network and $\|\theta\|$ represents both its norm and the polar angle of the ray corresponding to each pixel. The predicted FoV field is used to fit the camera model of choice. `division:i` corresponds to the division model with i distortion coefficients.

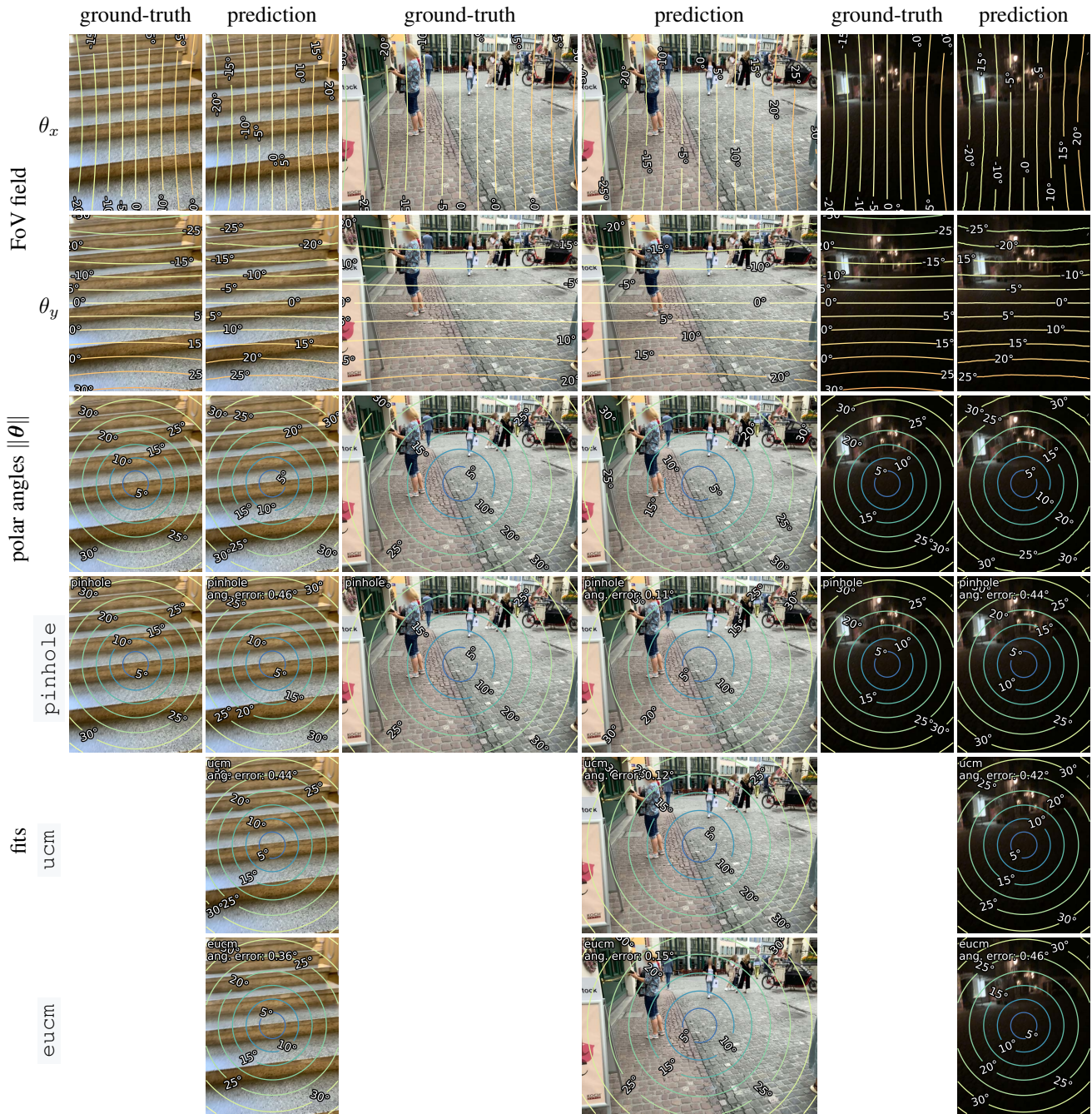


Figure 9. **Qualitative results on perspective images in LaMAR [69] with AnyCalib_{gen}**—trained on OP_g. The FoV field (θ_x and θ_y) is regressed by the network and $\|\theta\|$ represents both its norm and the polar angle of the ray corresponding to each pixel. The predicted FoV field is used to fit the camera model of choice.

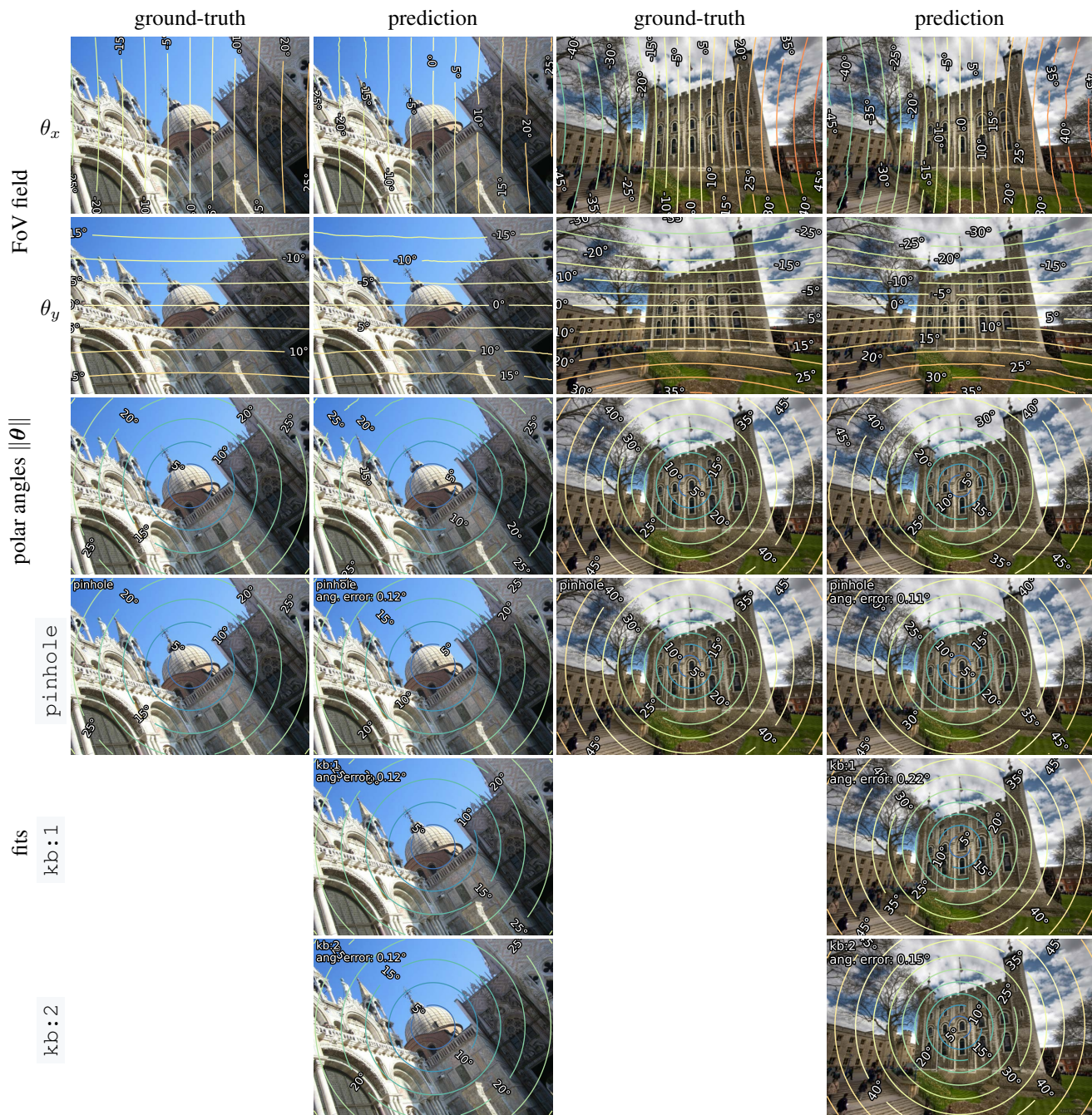


Figure 10. **Qualitative results on perspective images** in MegaDepth [49] with AnyCalib_{gen}—trained on OP_g. The FoV field (θ_x and θ_y) is regressed by the network and $\|\theta\|$ represents both its norm and the polar angle of the ray corresponding to each pixel. The predicted FoV field is used to fit the camera model of choice. kb: i corresponds to the Kannala-Brandt model with i distortion coefficients.

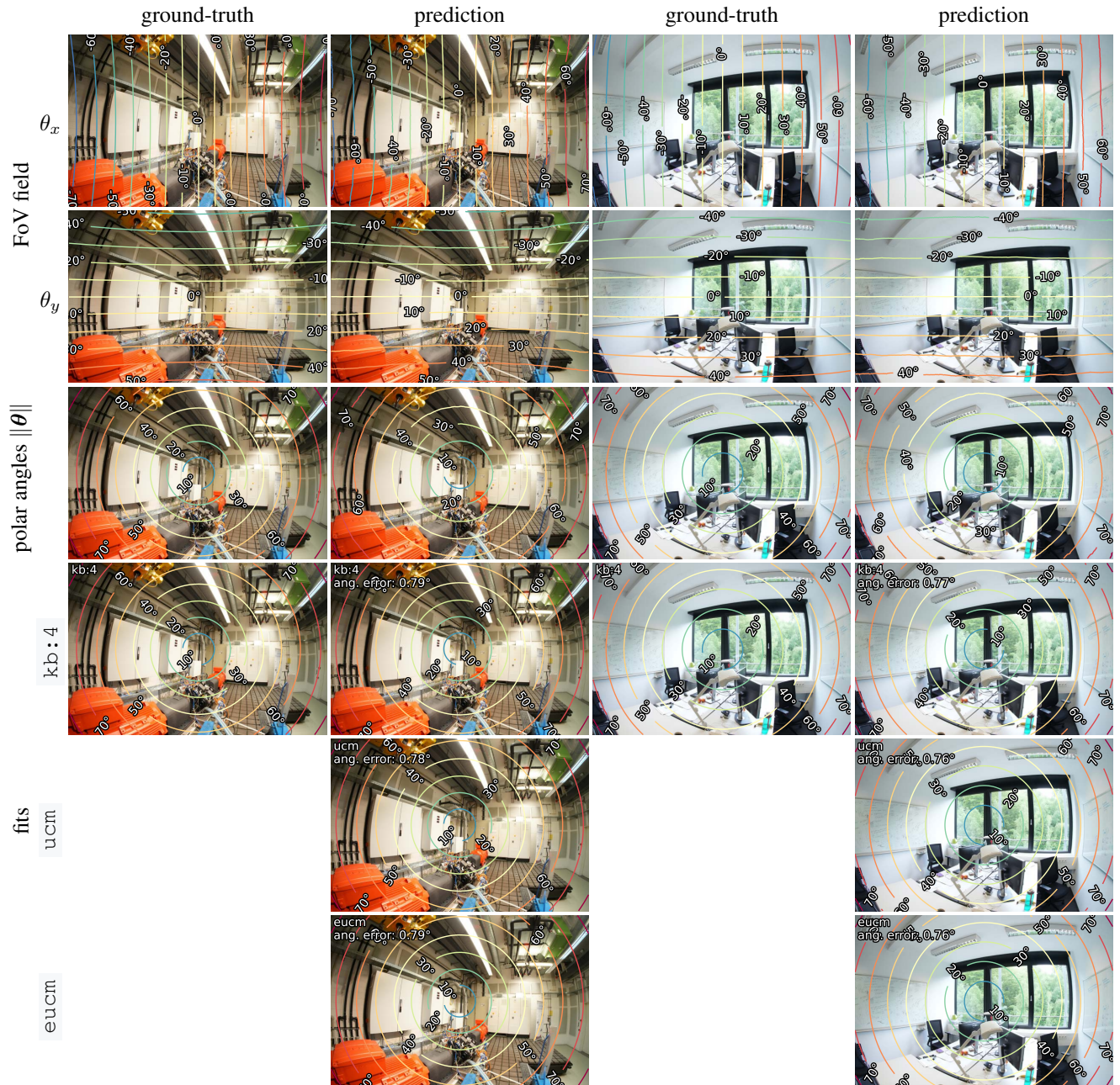


Figure 11. **Qualitative results on distorted images** in ScanNet++ [95] with AnyCalib_{gen}—trained on OP_g. The FoV field (θ_x and θ_y) is regressed by the network and $\|\theta\|$ represents both its norm and the polar angle of the ray corresponding to each pixel. The predicted FoV field is used to fit the camera model of choice. $kb:i$ corresponds to the Kannala-Brandt model with i distortion coefficients.

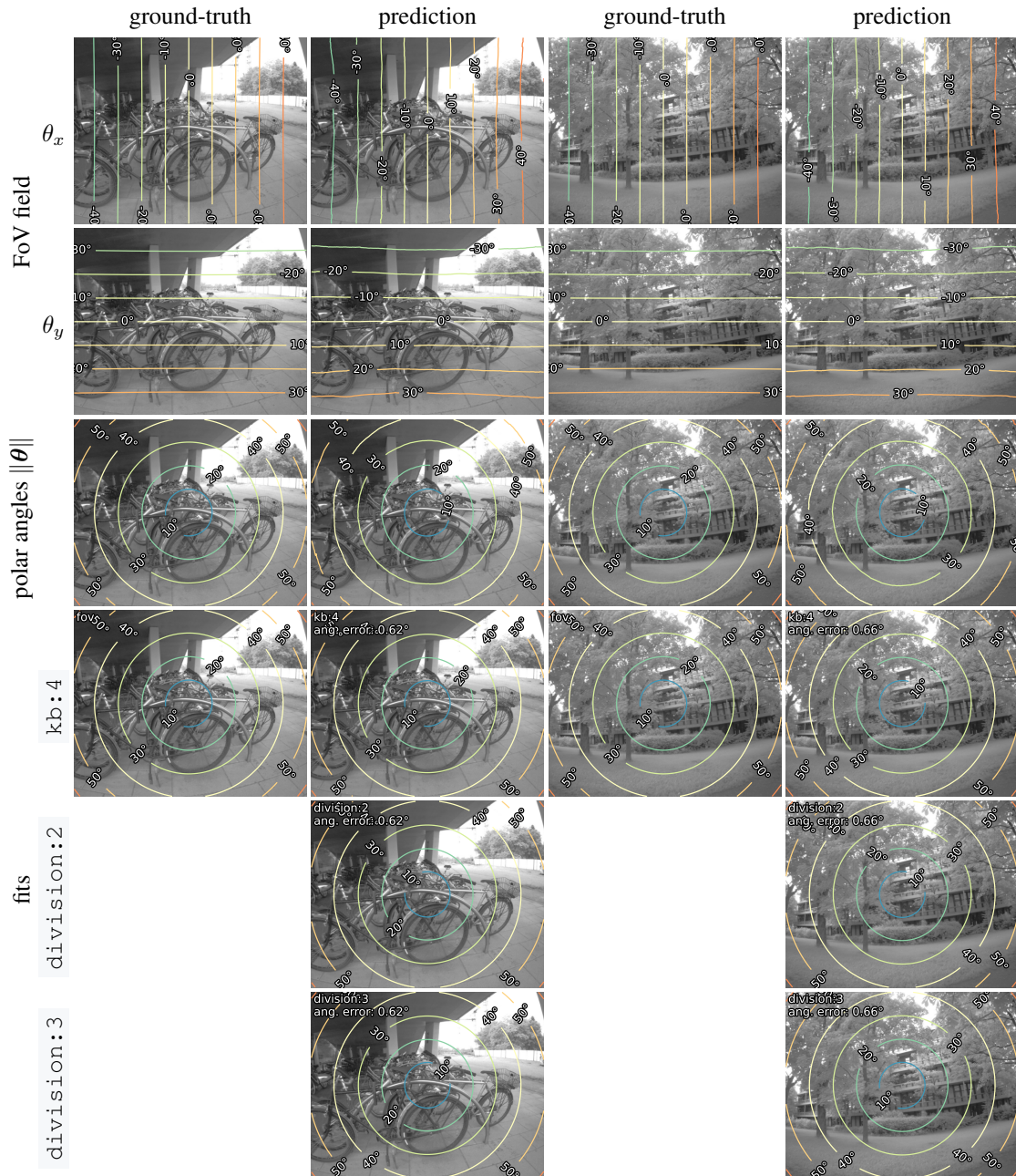


Figure 12. **Qualitative results on distorted images** in the Mono Dataset [23] with AnyCalib_{gen}—trained on OP_g. The FoV field (θ_x and θ_y) is regressed by the network and $\|\theta\|$ represents both its norm and the polar angle of the ray corresponding to each pixel. The predicted FoV field is used to fit the camera model of choice. `division:i` corresponds to the division model with `i` distortion coefficients.

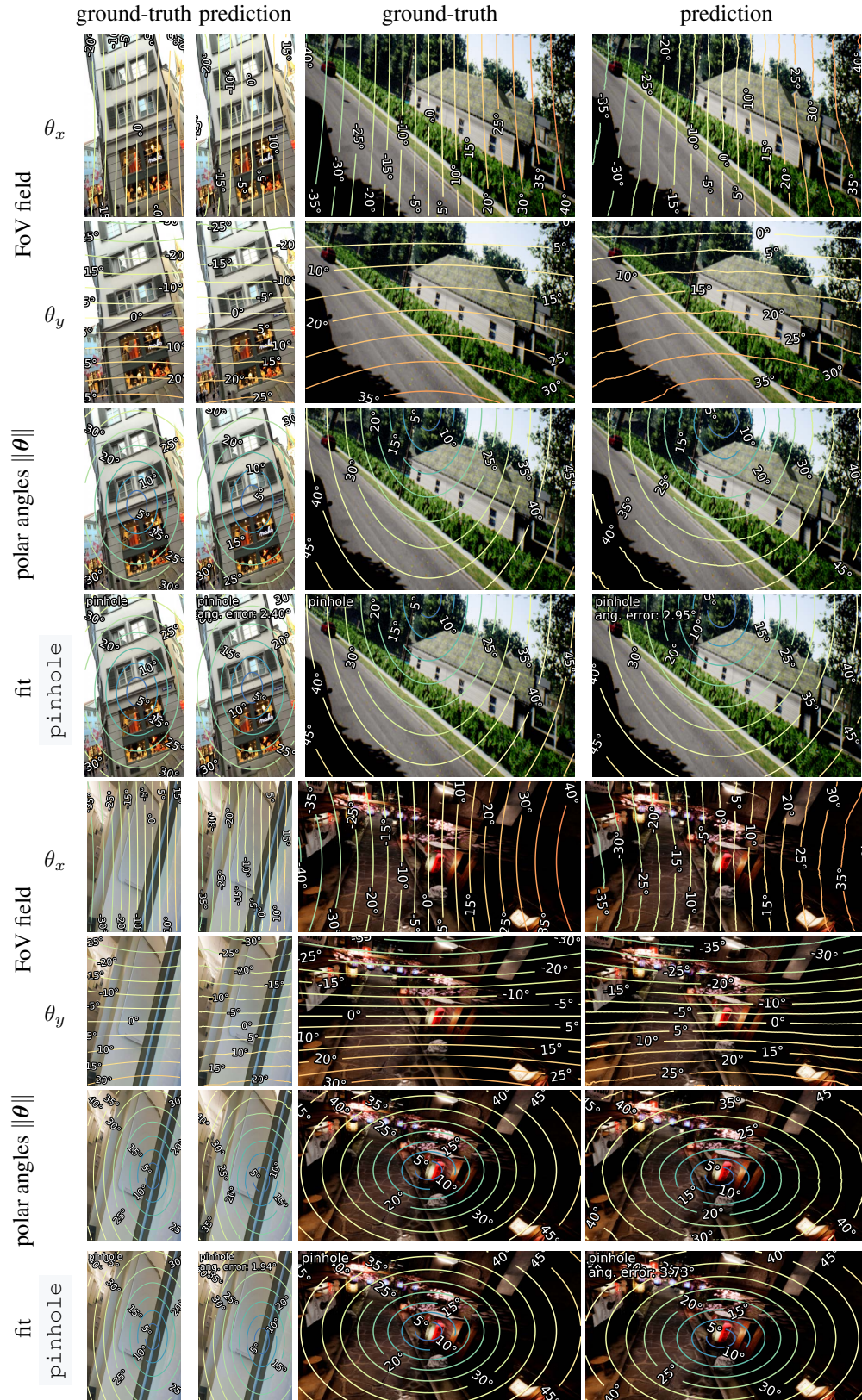


Figure 13. Qualitative results on edited images with AnyCalib being trained following [34, 100] (Sec. 3.3).

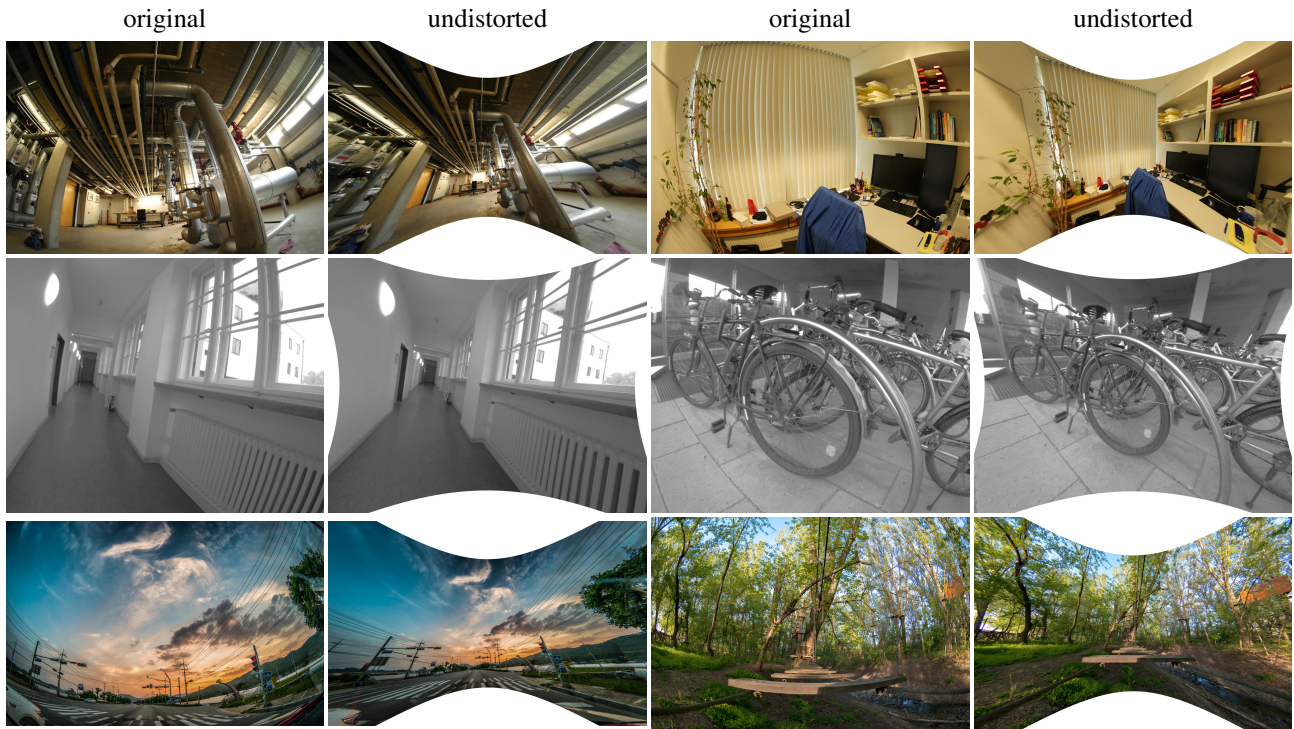


Figure 14. **Qualitative undistortion results** with AnyCalib_{gen} (trained on OP_g), on images from ScanNet++ [95] (top), Mono [23] (middle) and captured with a Samsung NX 10mm F3.5 Fisheye lens (bottom), provided by ExploreCams—authors: [crystal Yang](#) (left) and [Imre Farago](#) (right).